

The Supermassive Black Hole in the Nearby Spiral Galaxy M81: A Robust Mass from JWST/NIRSpec Stellar Dynamics

DIEU D. NGUYEN ,¹ TUAN N. LE ,² MICHELE CAPPELLARI ,³ HAI N. NGO ,² TINH Q. T. LE ,⁴ TIEN H. T. HO ,²
 LONG Q. T. NGUYEN ,² ELENA GALLO ,¹ FAN ZOU ,¹ MICHELE PERNIA ,⁵ NIRANJAN THATTE ,³ AND
 MIGUEL PEREIRA-SANTAELLA 

¹Department of Astronomy, University of Michigan, 1085 South University Avenue, Ann Arbor, MI 48109, USA

²Faculty of Physics – Engineering Physics, University of Science, Vietnam National University – Ho Chi Minh City, Vietnam

³Sub-Department of Astrophysics, Department of Physics, University of Oxford, Denys Wilkinson Building, Keble Road, Oxford, OX1 3RH, UK

⁴Department of Physics, International University, Vietnam National University in Ho Chi Minh City, Vietnam

⁵Centro de Astrobiología (CAB), CSIC–INTA, Departamento de Astrofísica, Cra. de Ajalvir Km. 4, 28850 – Torrejón de Ardoz, Madrid, Spain

⁶Instituto de Física Fundamental, CSIC, Calle Serrano 123, 28006 Madrid, Spain

(Received January 27, 2026)

Submitted to AAS Journals

ABSTRACT

Despite its proximity, the mass of the supermassive black hole (SMBH) in the spiral galaxy M81 (NGC 3031) has remained uncertain, with previous dynamical measurements being unreliable. We present the first robust stellar-dynamical measurement of its mass using high-resolution, two-dimensional kinematics from *JWST/NIRSpec* observations of the central $3'' \times 3''$. By tracing stellar motions in the near-infrared, our data penetrate the obscuring nuclear dust and allow for the separation of stellar light from the non-thermal AGN continuum. We modeled the kinematics using JAM within a Bayesian framework, exploring a comprehensive suite of models that systematically account for uncertainties in the point-spread function, orbital anisotropy, and stellar mass-to-light ratio. This ensemble modeling approach demonstrates that a central dark mass unambiguously drives the central rise in velocity dispersion. The models yield a robust SMBH mass of $M_{\text{BH}} = (4.78^{+0.07}_{-0.10}) \times 10^7 M_{\odot}$. This result resolves a long-standing uncertainty in the mass of M81’s black hole and provides a crucial, reliable anchor point for SMBH-galaxy scaling relations.

Keywords: Astrophysical black holes (98) — Galaxy kinematics (602) — Galaxy dynamics (591) — Galaxy nuclei (609) — Galaxy spectroscopy (2171) — Astronomy data modeling (1859)

1. INTRODUCTION

The masses of supermassive black holes (SMBHs; $M_{\text{BH}} \approx 10^{6-10} M_{\odot}$) are known to correlate tightly with the global properties of their host galaxies, establishing a fundamental link between their evolution. These scaling relations, such as the $M_{\text{BH}}-\sigma$ relation, have been established and refined in numerous studies (e.g., K. Gultekin et al. 2009; N. J. McConnell & C.-P. Ma 2013; R. P. Saglia et al. 2016; R. C. E. van den Bosch 2016), and are comprehensively reviewed in J. Kormendy & L. C. Ho (2013). Accurately measuring M_{BH} is crucial for calibrating these scaling relations, but it remains a significant observational challenge. The most reliable mea-

surements are derived from dynamical modeling of the gravitational potential, using the motions of various tracers. These include stars (e.g., E. K. Verolme et al. 2002; K. Gebhardt et al. 2003; M. Cappellari et al. 2009; J. L. Walsh et al. 2016; C. P. Ahn et al. 2018; D. Krajnović et al. 2018; K. T. Voggel et al. 2018; D. D. Nguyen et al. 2014, 2017, 2018, 2019; D. D. Nguyen 2017; S. Thater et al. 2019, 2022, 2023), ionized gas (e.g., A. J. Barth et al. 2001; K. L. Shapiro et al. 2006; N. Neumayer et al. 2007), and molecular gas (e.g., T. A. Davis et al. 2013; K. Onishi et al. 2017; T. A. Davis et al. 2020; D. D. Nguyen 2019; D. D. Nguyen et al. 2020, 2021, 2022; H. N. Ngo et al. 2025b).

The nearby spiral galaxy M81 (NGC 3031) is a prime example of the difficulties in measuring BH masses. Throughout this paper, we adopt a distance of $D = 3.63 \pm 0.14$ Mpc (P. R. Durrell et al. 2010). This value represents the mean of five independent determinations: one based on Cepheid variables

Corresponding author: Dieu D. Nguyen
 dieun@umich.edu

(W. L. Freedman et al. 1994; L. Ferrarese et al. 2000; L. P. McCommas et al. 2009) and four derived from the Tip of the Red Giant Branch (TRGB) method (N. A. Tikhonov & O. A. Galazutdinova 2005; L. Rizzi et al. 2007; J. J. Dalcanton et al. 2009; P. R. Durrell et al. 2010).

Despite its proximity, a reliable measurement of the SMBH mass in M81 has remained elusive. To date, only two direct dynamical modelling determinations have been attempted, but they are both problematic (see discussion in the box at pg. 552 of the review by J. Kormendy & L. C. Ho 2013). The first attempt was a preliminary stellar-dynamical measurement and BH discovery, based on a two-integral Jeans model of long-slit *HST/STIS* observations (G. A. Bower et al. 2000), which is known to be an overly restrictive assumption for realistic galaxies. This preliminary value $M_{\text{BH}} = 6(\pm 20\%) \times 10^7 M_{\odot}$ was never finalized or published in a peer-reviewed paper, and the abstract in the AAS Bulletin did not include any figures. The other determination was based on ionized gas kinematics, which yielded an estimate of $M_{\text{BH}} = (7 \pm 2) \times 10^7 M_{\odot}$ (N. Devereux et al. 2003). However, the underlying gas velocity field appears highly disturbed and is poorly represented by the regular rotating disk model assumed in that work (see their Figure 2), casting significant doubt on the accuracy of the result. Consequently, our work provides the first reliable and detailed measurement of the M_{BH} in this galaxy. This large uncertainty is compounded by the presence of a low-luminosity active galactic nucleus (LLAGN; M. Eracleous et al. 2010) and complex dust structures associated with both inflows (A. Schnorr Müller et al. 2011) and outflows (F. Shi et al. 2021), which can significantly bias measurements made at optical wavelengths (S. Thater 2019).

The advent of the *James Webb Space Telescope (JWST)* offers a transformative opportunity to overcome these challenges. By targeting the CO bandhead absorption features in the near-infrared (NIR) at $\sim 2.3 \mu\text{m}$, the NIRSpec instrument can trace stellar motions directly, penetrating the obscuring dust that affects optical studies (e.g., M. Cappellari et al. 2009). Adopting a velocity dispersion of $\sigma = 162 \text{ km s}^{-1}$ (A. Schnorr Müller et al. 2011) the $M_{\text{BH}} - \sigma$ relation by K. Güttekin et al. (2009) predicts a $M_{\text{BH}} \approx 5 \times 10^7 M_{\odot}$. Given this mass, the SMBH's sphere of influence (SOI) is $r_{\text{SOI}} \approx 0''.5$. This is more than three times the NIRSpec point spread function (PSF) full width at half maximum (FWHM) at this wavelength (F. D'Eugenio et al. 2023; F. D'Eugenio et al. 2025), ensuring the gravitational influence of the black hole is well-resolved. These capabilities are crucial for probing the demographic of intermediate-mass black holes (IMBHs, $M_{\text{BH}} \approx 10^{2-5} M_{\odot}$) and bona-fide massive BHs ($M_{\text{BH}} > 1.8 \times 10^7 M_{\odot}$; G. Sasseville et al. 2024), a regime that will be further explored by next-generation facilities like the 39-meter extremely large telescope (ELT; e.g.,

D. D. Nguyen et al. 2023, 2025a; H. N. Ngo et al. 2025a; H. N. Ngo et al. 2025; N. A. Thatte et al. 2024).

In this work, we measure the stellar-based SMBH mass in M81 using Jeans Anisotropic Models (JAM; M. Cappellari 2008, 2020) applied to archival *JWST/NIRSpec G235H/F170LP IFU* data (PID: 02016, PI: Anil C. Seth), *HST/Wide Field Camera 3 (WFC3)* infrared (IR) F110W-band imaging (PID: 11421, PI: H. A. Bushouse), and the *J*-band image from the Two Micron All Sky Survey (2MASS) (T. H. Jarrett et al. 2003). The modeling also constrains key dynamical parameters, including inclination, anisotropy, and the stellar mass-to-light ratio (M/L_J), and assesses their impact on the inferred M_{BH} (e.g., D. D. Nguyen et al. 2018, 2019) in M81.

It is important to note that the nucleus of M81 exhibits dust structures associated with both inflows (A. Schnorr Müller et al. 2011) and outflows (F. Shi et al. 2021), which can bias optical gas-dynamical measurements (S. Thater 2019). The NIRSpec G235H/F170LP observations mitigate these effects by targeting the CO bandhead absorption lines (e.g., M. Cappellari et al. 2009) in the NIR, where dust extinction is minimal and stellar motions are traced directly. Thus, our measurements not only refine the M_{BH} estimate for M81, but also demonstrate the remarkable capability of *JWST/NIRSpec* to probe SMBH demographics.

This paper is organized as follows. In Section 2, we describe the NIRSpec IFU observations, the data reduction, the correction of spectral wiggles in the central regions, and the extraction of the two-dimensional (2D) line-of-sight velocity distribution (LOSVD) from the CO bandhead features. Section 3 details the construction of the stellar photometric model from the *HST* F110W and 2MASS *J*-band images. In Section 4, we combine the 2D LOSVD and photometric model as input for JAM models to derive M_{BH} . Finally, our results and conclusions are presented in Section 6.

2. JWST/NIRSPEC OBSERVATIONS AND KINEMATICS

2.1. G235H/F170LP IFU Data

M81 was observed on 25 November 2022 with the *JWST/NIRSpec* IFU using the high spectral resolution grating (G235H/F170LP; $R \sim 2700$), covering the wavelength range between $1.66\text{--}3.17 \mu\text{m}$ and a spectral sampling of 4 \AA per spectral pixel. This observation employed the NR-SIRS2RAPID readout pattern with 14 groups per integration and one integration per exposure, with an effective integration time of 204 seconds and a total effective exposure time of 1,634 seconds. A four-point medium-cycling dither pattern was used to optimize spatial sampling. The raw data were processed using the *JWST* calibration pipeline, specifically STScI pipeline version v1.14.0 (H. Bushouse et al. 2024) with the Calibration Reference Data System (CRDS) con-

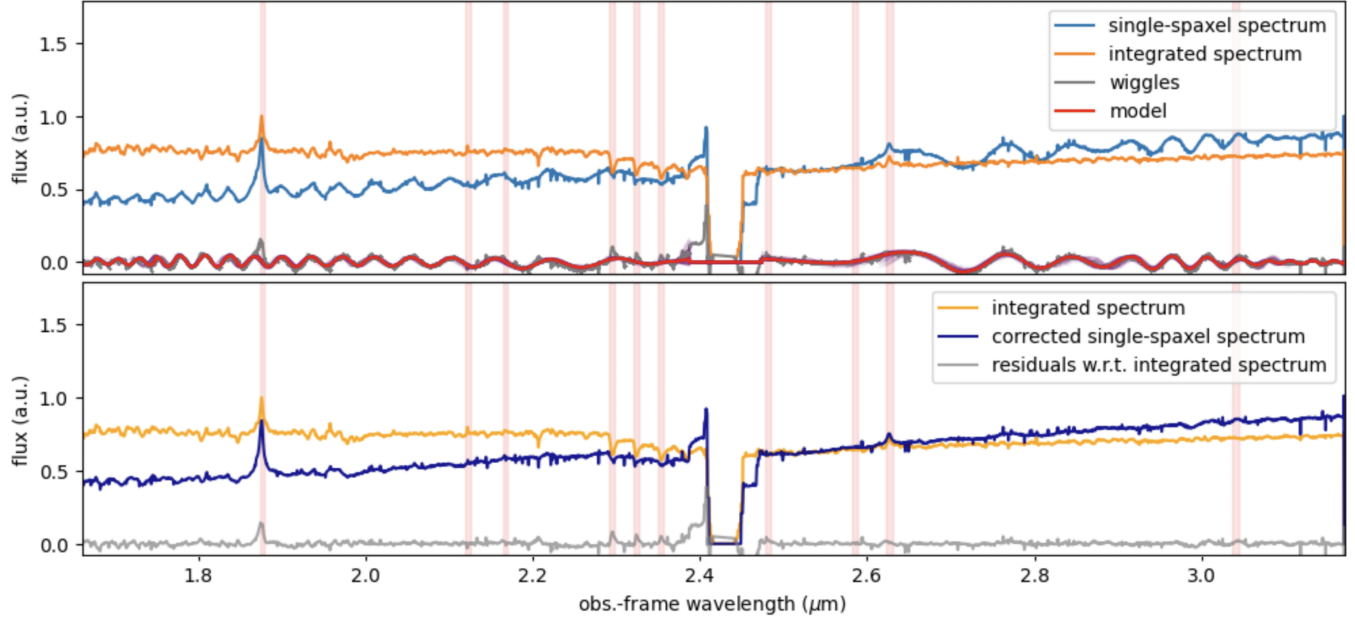


Figure 1. Modeling of wiggles in the single-spaxel NIRSpec spectrum of M81. *Top panel:* Integrated spectrum (orange), single-spaxel spectrum (blue), and residual wiggles (gray). The red curve shows the best-fitting wiggle model. *Bottom panel:* Wiggle-corrected single-spaxel spectrum (dark blue) compared to the integrated spectrum (orange); residuals after correction are shown in gray. In all panels, red shaded regions mark emission lines excluded from the fit.

text `jwst_1242.pmap`⁷. The final datacube was resampled at a pixel scale of $0''.1$, approximately five times smaller than the SMBH’s r_{SOI} (as discussed in Section 1), and covers the central field of view (FoV) of $3'' \times 3''$.

2.2. Wiggles Corrections

Under-sampling of the NIRSpec PSF introduces sinusoidal artifacts, commonly referred to as “wiggles,” into individual spaxel spectra of bright sources. These features are largely mitigated when spectra are integrated over apertures of approximately $0''.2$ – $0''.5$ (D. R. Law et al. 2023). Because the standard NIRSpec pipeline does not provide a built-in correction for these artifacts, we employed the empirical routine developed by M. Perna et al. (2023)⁸. The method is briefly summarized below.

First, we extracted the spectrum from the brightest spaxel, where wiggles are most prominent, and masked intrinsic emission lines, absorption features, and the spectral gap between the two NIRSpec detectors. We then fit a sinusoidal model within rolling wavelength windows iteratively, allowing the fit to adapt locally to wavelength-dependent variations in wiggle characteristics as shown in Figure 1. This model was calibrated against the spectrum extracted from a 4-pixel-radius ($0''.4$) circular aperture, centered on the peak of the white-light image, where wiggles are effectively smoothed out. We found that this aperture is sufficient to suppress

wiggles in the NIRSpec IFS data cube of M81. Finally, the resulting wiggle frequency was adopted as a prior when subtracting the oscillations from all other affected spaxels.

All subsequent analyses were performed using the wiggle-corrected data cube.

2.3. Defining the Galaxy Center

Because the kinematic center is less precisely constrained due to its reliance on LOSVD extractions (Section 2.7), we adopted the more accurate photometric center, defined as the weighted barycenter of the ~ 150 brightest pixels, under the assumption that the black hole coincides with the surface-brightness peak. This photometric, AGN-aligned center was used as the origin in all models and figures.

2.4. Stellar Kinematics Templates and pPXF Setup

As the nucleus of M81 is classified as a LLAGN (M. Eracleous et al. 2010), its nuclear spectra likely contain a substantial contribution from AGN continuum emission in several central spaxels (see Section 2.2). This continuum emission dilutes the stellar CO bandhead absorption features used to trace stellar kinematics, resulting in underestimated velocity dispersions and reduced line strength (γ ; see Section 2.2 of R. P. van der Marel & M. Franx 1993). Additionally, a rising continuum can mimic changes in the stellar population, biasing the template mix and further reducing the reliability of the velocity-dispersion measurement.

Following M. Cappellari et al. (2009); D. A. Simon et al. (2024); D. D. Nguyen et al. (2025b), we defined the observed

⁷ <https://jwst-crds.stsci.edu>

⁸ https://github.com/micheleperna/JWST-NIRSpec_wiggles

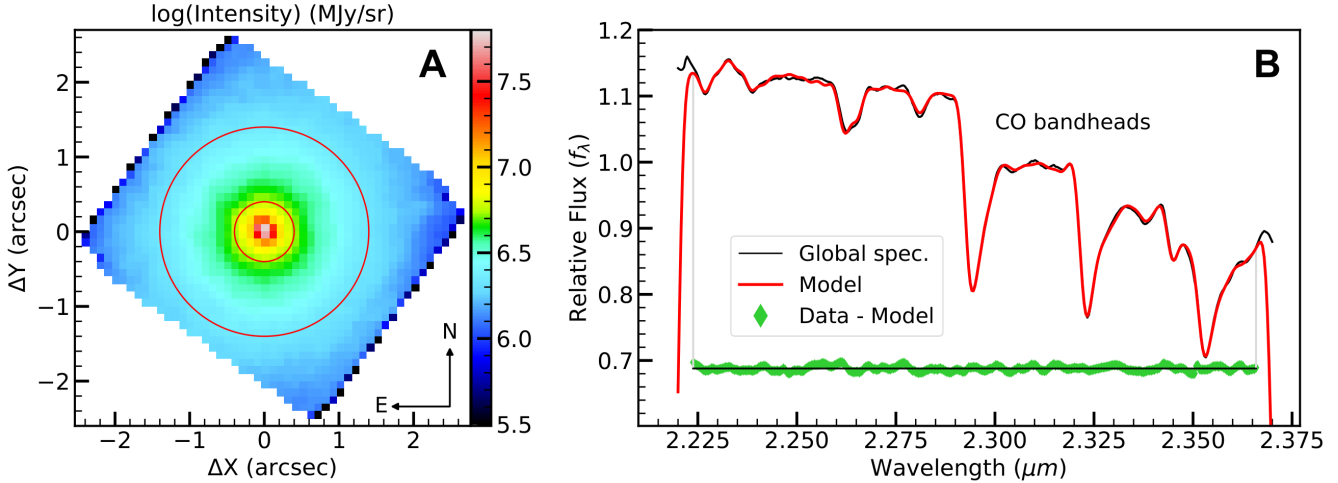


Figure 2. *Panel A:* Logarithmically scaled intensity map of the NIRSpec G235H/F170LP data cube, collapsed along the spectral axis (excluding the detector gap at 2.41 – $2.49\ \mu\text{m}$). The red circular annulus ($0\farcs4 < r < 1\farcs4$) indicates the region from which the global spectrum was extracted. *Panel B:* The observed global spectrum (black) overlaid with the best-fit stellar template (red) for M81. The fit residuals (data – model) are shown in green and vertically offset by $+0.62$ to compress the y -axis range and better illustrate the stellar CO absorption bandheads. This same vertical offset is applied to all subsequent figures of this type.

line-strength as $\gamma = \text{stars}/(\text{stars} + \text{AGN})$, representing the fraction of flux attributed to the stellar template within the fitted spectral range. At large distances from the nucleus, $\gamma \approx 1$ when continuum contamination is negligible. Toward the center, γ decreases below unity and drops sharply in the innermost spaxels where the AGN continuum dominates.

Stellar kinematics were extracted from the *JWST*/NIRSpec G235H/F170LP data cube of M81 using the Penalized PiXel-Fitting (pPXF) method⁹ (M. Cappellari & E. Emsellem 2004; M. Cappellari 2017, 2023), focusing on the commonly-used CO bandhead absorption features (e.g., M. Cappellari et al. 2009; D. D. Nguyen et al. 2018; D. Krajnović et al. 2018; S. Thater et al. 2023). As demonstrated by D. D. Nguyen et al. (2025c,b), LOSVDs derived using the empirical X-shooter Spectral Library (XSL; 830 spectra from 683 stars¹⁰; K. Verro et al. 2022) agree within 3% of those obtained from the higher-resolution PHOENIX synthetic library (T.-O. Husser et al. 2013). The LOSVD based on XSL is thus adopted as our primary kinematic measurements throughout our analysis. The XSL covers 3000–25,000 Å at $R \sim 10,000$, includes O–M and evolved stars, and has been corrected for extinction.

We followed the method of M. Cappellari et al. (2009) to separate the stellar light from the non-thermal AGN continuum in the nucleus of M81. This process requires an optimal XSL template, derived from a large spatial region of the nucleus to avoid kinematic bias (A. Marconi et al. 2000; J. D. Silge & K. Gebhardt 2003) caused by the AGN

continuum. The stellar continuum was modeled using fourth-degree additive (degree = 4) and multiplicative (mdegree = 4) Legendre polynomials within pPXF, as this configuration provided the most stable LOSVD after testing various combinations of degree and mdegree values between 4 and 8. The resulting LOSVDs are nearly identical beyond $0\farcs2$, with differences within this radius remaining below 7.5%. These polynomials effectively capture low-order variations in line strength, residual sky-subtraction errors, spectral calibration imperfections, and AGN continuum contamination, allowing for robust measurements of the stellar velocity dispersion even in the central spaxels where AGN light dominates over the stellar CO bandheads.

2.5. Determining the Optimal Stellar Template

First, we constructed a global spectrum by combining all spaxels within an annulus of $0\farcs4 < r < 1\farcs4$ (confined by the two red rings in the left panel of Figure 2) of the NIRSpec G235H/F170LP data cube, thereby excluding the central, AGN-contaminated spaxels. This annular spectrum achieves a signal-to-noise ratio (S/N) of 300 per spectral pixel and was logarithmically rebinned along the spectral dimension with a constant velocity scale of $50\ \text{km s}^{-1}$ per pixel calculated using Eq. 8 of M. Cappellari (2017).

Second, we accounted for the instrumental broadening of the spectrum in the XSL templates by convolving them with a Gaussian whose dispersion is determined using Eq. 5 of M. Cappellari (2017).

Third, we derived the fixed optimal XSL template by fitting the XSL-instrumental-broadened spectra to the global spectrum using pPXF, modeling the LOSVD as a simple Gaussian by setting moments = 2. This setup returns the LOSVD pa-

⁹ v8.2.1: <https://pypi.org/project/pxxf/>

¹⁰ Data Release 3: <http://xsl.u-strasbg.fr>

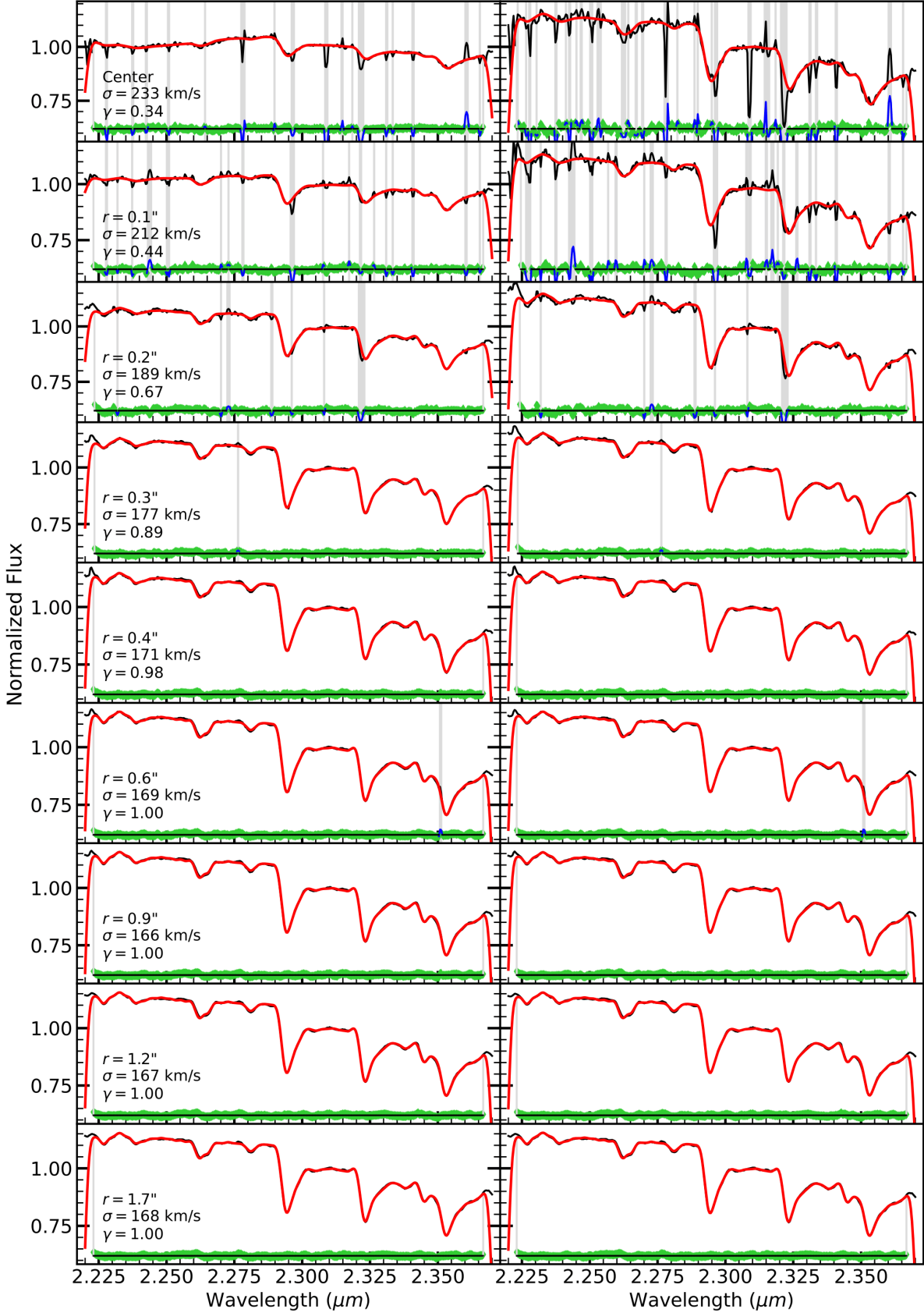


Figure 3. Radial spectral variation in M81 from the NIRSpec G235H/F170LP data cube. *Left column:* Observed spectra (black line) obtained by coadding spaxels within concentric annuli at radius r . The overplotted red line shows the pPXF fit, which combines the global stellar template (see left panel of Figure 2 and Section 2.4), convolved with a Gaussian LOSVD and added by fourth-degree additive and multiplicative polynomials to account for the non-thermal nuclear continuum. Fit residuals (data-model) are shown in green, with regions masked due to emission lines or artifacts indicated in gray. *Right column:* The convolved stellar template (red line) is compared to the observed spectrum after subtracting of the modeled non-thermal continuum (black line).

rameters, including the rotational velocity V (relative to the systemic velocity V_{sys}) and the velocity dispersion σ , which are our primary kinematic quantities of interest.

The fixed optimal XSL template, returned by pPXF, is composed of 14 giant-star spectra, which reproduce the observed spectrum over 2.22–2.37 μm , including the CO bandhead absorption (right panel of Figure 2). The fit is dominated by the K4III C star (HD 109871 from XSL), contributing $\approx 45\%$ of the flux, with additional contributions from a giant M2V C star (HIP 75423, $\approx 18\%$) and an M9 D star (BMB 289, $\approx 10\%$) required to match the data. From this template, pPXF yields $V = -31 \pm 3 \text{ km s}^{-1}$ and $\sigma = 168 \pm 4 \text{ km s}^{-1}$, consistent with long-slit measurements at Calar Alto Observatory (R. Bender et al. 1994). The 1σ uncertainties are estimated from the standard deviation of 200 Monte Carlo realizations (M. Cappellari & E. Emsellem 2004).

2.6. Separating AGN Continuum from Stellar Light

In this section, we assess the reliability of the fixed optimal stellar template (Section 2.4) for extracting stellar kinematics in the presence of non-thermal AGN emission within the NIRSpec G235H/F170LP data cube. To do so, we constructed high-S/N spectra by coadding spaxels within multiple concentric annuli spanning radii from $0''.1$ to $1''.7$. Each annular spectrum was then fit using the fixed optimal stellar template within the pPXF framework.

Figure 3 shows the radial profiles of stellar line strength (γ , left) and stellar-light fraction (right). The observed spectra in each annulus are modeled with the fixed optimal stellar template plus fourth-degree additive and multiplicative Legendre polynomials to account for AGN continuum emission. The stellar-light fraction (right panels) is obtained by subtracting the AGN component, revealing a clear non-stellar contribution from the changing spectral slope. In the nucleus, the AGN contributes 66% of the flux, decreasing to $\approx 54\%$ at $r \approx 0''.1$, $\approx 33\%$ at $r \approx 0''.2$, and $< 10\%$ beyond $r = 0''.2$.

We quantify the dilution of stellar light by the central nonthermal AGN continuum in Figure 4, which presents the radial surface-brightness profile $I(r)$ measured from the JWST/NIRSpec G235H/F170LP data cube of M81, together with the stellar contribution $\Gamma(r) = I(r)\gamma(r)$ derived from the pPXF fits in individual spatial bins. Similar analyses have been carried out for nearby systems such as M87 (Figure 4 of R. P. van der Marel 1994), Centaurus A (Figure 6 of M. Cappellari et al. 2009), and more recently M106 (Figure 4 of D. D. Nguyen et al. 2025b). As an initial approximation in Figure 4, we modeled the radial stellar-light distribution using a single power-law form, $\Gamma(r) = \alpha \times r^\beta$ (red line), with $\alpha = 0.04$ and $\beta = -0.82$. This simple model overestimates the stellar-light fraction within $0''.1$ (blue dashed line), as it neglects the effect of the JWST/NIRSpec PSF at $2.3 \mu\text{m}$.

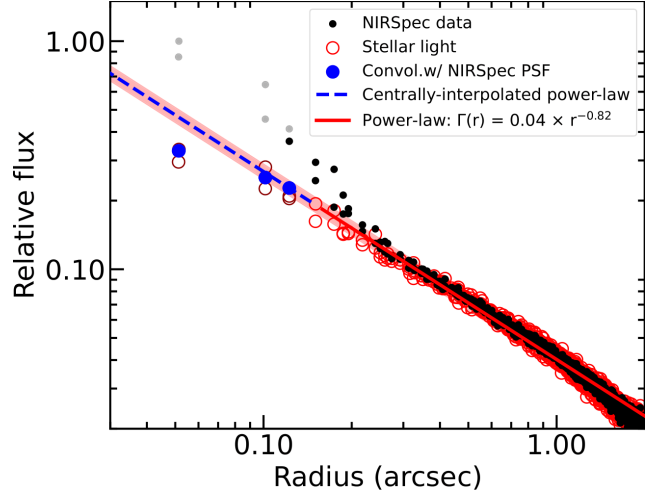


Figure 4. The radial surface brightness profile $I(r)$, derived from individual Voronoi bins in the NIRSpec G235H/F170LP data cube of M81 (filled black circles), is compared to the estimated stellar light profile $\Gamma(r) = I(r)\gamma(r)$ (red open circles). The underlying stellar distribution is smooth and well approximated by a single-power-law (red line with pink region shows its 1σ uncertainty). The PSF-convolved central interpolation of this single power-law also reproduces the two innermost γ measurements, which lie below the intrinsic (unconvolved) profile, indicating that their apparent decline is fully consistent with PSF effects. Gray points indicate pixels where $\gamma < 0.5$.

To assess the impact of PSF convolution, we performed a forward-modeling experiment. First, we generated a synthetic image with an intrinsic surface-brightness profile $\Sigma \propto r^{-0.82}$, sampled at $0''.025 \text{ pixel}^{-1}$, corresponding to a factor of four oversampling relative to the native NIRSpec spatial scale (PSF 1 in Table 1 of D. D. Nguyen et al. 2025b). This image was then convolved with the synthetic NIRSpec PSF at the same sampling and subsequently rebinned to the native scale of $0''.1 \text{ pixel}^{-1}$ by summing 4×4 spaxels. We then measured the stellar fraction in the central spaxel of the rebinned image.

The resulting central stellar fraction follows the same trend defined by the three innermost measurements of $\gamma(r)$ in Figure 4, demonstrating that the apparent break toward the nucleus is fully accounted for by PSF convolution and spatial sampling effects. This behavior does not imply a genuine change in the intrinsic stellar surface-brightness profile within the NIRSpec FoV, but rather reflects instrumental effects that are properly accounted for once the PSF is taken into consideration. The determination of $\gamma(r)$ therefore enables a robust extraction of stellar kinematics even in the unresolved nuclear region, where stellar light is strongly diluted by AGN emission.

Although stars contribute only $\sim 34\%$ of the total flux in the central spaxel, the resulting kinematics remain usable, albeit with larger systematic uncertainties of order $\sim 15\%$, and are thus retained in our dynamical modeling (Section 4.1).

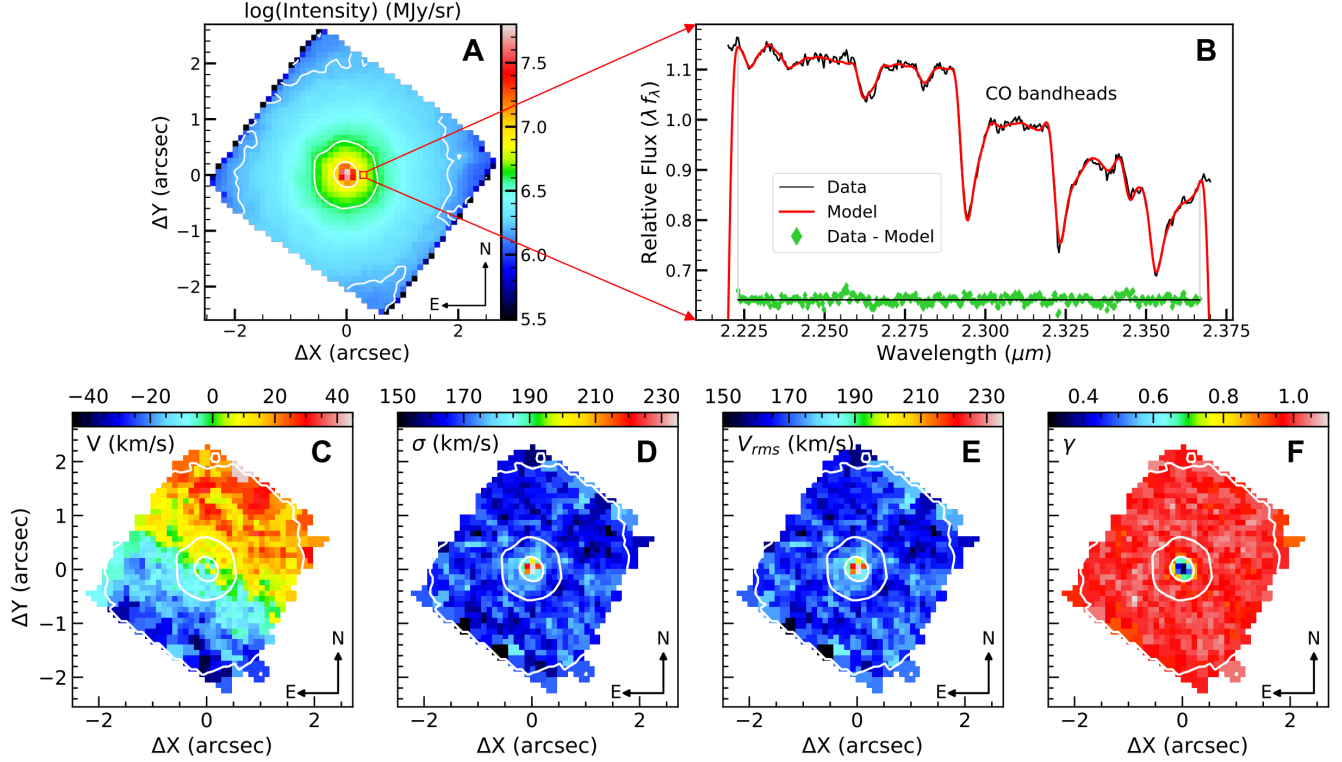


Figure 5. Stellar kinematic measurements from the NIRSpec G235H/F170LP observations of NGC 3031 are shown. *Panel A*: The logarithmic collapsed intensity map (cf. left panel of Figure 2). *Panel B*: Example pPXF fit for a central-offset Voronoi bin unaffected by wiggles (location indicated in Panel A). The observed spectrum (black) displays the CO bandhead absorptions near $2.3 \mu\text{m}$, with the best-fit XSL template overplotted in red. Fit residuals (data - model) are plotted in green, and the vertical gray lines mark the wavelength range used for fitting across all bins. *Panels C–F*: 2D maps of the stellar rotation velocity (V), velocity dispersion (σ), root-mean-square velocity ($V_{\text{rms}} = \sqrt{V^2 + \sigma^2}$), and stellar light contribution fraction (γ). The central white pixels are masked due to unreliable kinematics, as the AGN continuum contributes $\approx 66\%$ of the total light in this region. White contours trace the intensity, decreasing by $\text{mag arcseconds}^{-1}$ steps from the center.

At radii beyond $r = 0''.1$, the stellar contribution increases and the kinematic measurements are correspondingly more secure, with typical uncertainties below 3%.

2.7. Two-Dimensional Kinematic Maps

The 2D stellar LOSVD of the nucleus of M81 was derived following the fitting procedure described in Section 2.4. First, the adaptive Voronoi binning method¹¹ (M. Cappellari & Y. Copin 2003) was applied to spatially group spaxels until a target S/N of 150 per spectral pixel was achieved, resulting in $N = 700$ Voronoi bins. This target S/N represents a compromise: spaxels beyond $r \approx 0''.5 \approx r_{\text{SOI}}$ were grouped, while those within this radius remained unbinned to preserve the spatial resolution necessary for precise stellar kinematic measurements inside r_{SOI} . Within the SOI, individual unbinned spaxels exhibit S/N values ranging from 150 to 200 per spectral pixel, increasing toward the central peak. Each binned spectrum was resampled onto a logarithmic wavelength scale. The pPXF routine was then used to fit each binned spectrum

Table 1. JWST/NIRSpec Kinematic Data of the M81 Nucleus

$\Delta\text{R.A.}$ ($''$)	$\Delta\text{Decl.}$ ($''$)	V (km s^{-1})	ΔV (km s^{-1})	σ (km s^{-1})	$\Delta\sigma$ (km s^{-1})
0.012	0.050	7.66	14.16	233.77	14.05
0.112	0.050	-9.08	6.79	216.17	8.66
0.012	-0.150	-11.06	5.02	180.76	6.33
0.212	0.050	10.43	3.76	179.11	4.72
-0.188	0.150	8.23	3.82	188.36	4.80
-0.088	-0.250	-12.29	3.46	174.71	4.33
-0.288	-0.050	-9.06	3.29	172.81	4.12
...

(This table is available in its entirety in machine-readable form. A portion is shown here for guidance regarding its form and content. A data copy is also available in Zenodo at doi: 10.5281/zenodo.18345300)

with the fixed optimal XSL-instrumental-broadened template (Section 2.5), incorporating fourth-degree multiplicative and additive Legendre polynomials to derive the LOSVD (i.e., V and σ).

¹¹ v3.1.5: <https://pypi.org/project/vorbin/>

Figure 5 presents the logarithmic integrated intensity map (panel A), with a marked spaxel corresponding to the spectrum and pPXF fit shown in panel B. The remaining panels display the resulting maps of rotational velocity V (panel C), velocity dispersion σ (panel D), root-mean-square velocity $V_{\text{rms}} = \sqrt{V^2 + \sigma^2}$ (panel E), and stellar line strength γ (panel F). The nucleus exhibits a steeply rising rotation, with $|V| \approx 40 \pm 4 \text{ km s}^{-1}$ at the edge of the NIRSpec IFU field (after subtracting the systemic heliocentric velocity of $v_{\text{sys}} = -32 \pm 4 \text{ km s}^{-1}$), consistent with the IFS observations by A. Schnorr Müller et al. (2011), as expected for a spiral galaxy. This derived v_{sys} from the *JWST*/NIRSpec G235H/F170LP data cube is 7 km s⁻¹ larger than that value reported in the NASA/IPAC Extragalactic Database (NED¹²).

We measure a global kinematic position angle of $\text{PA}_{\text{kin}} = 151.6^\circ \pm 9.5^\circ$. Both v_{sys} and PA_{kin} were derived from the velocity map using the pafit¹³ package (D. Krajnović et al. 2006). The kinematic PA_{kin} is consistent within the uncertainties with the photometric one $\text{PA}_{\text{phot}} \approx 157^\circ$ reported in the HyperLeda database¹⁴ (G. Paturel et al. 2003), as expected for a nearly axisymmetric disk galaxy. The σ profile, which dominates over V , rises from $\sim 165 \pm 4 \text{ km s}^{-1}$ at $r \gtrsim 1''$ ($\approx 3 \text{ km s}^{-1}$ higher than the value obtained from GMOS observations by A. Schnorr Müller et al. 2011), to a central peak of $\sim 233 \pm 15 \text{ km s}^{-1}$ within $r \lesssim 0''.1$. This central increase in both σ and V_{rms} provides strong evidence for the presence of a central SMBH. We presented these stellar-kinematic measurements in Table 1.

As shown in panel F of Figure 5, the non-thermal AGN continuum exhibits only weak emission, with $\gamma \approx 1$ over most of the NIRSpec FoV, except within the innermost spaxels where $\gamma \leq 0.34$. In these central spaxels, the AGN light dominates, resulting in relatively large kinematic uncertainties of up to $\sim 15\%$. In contrast, for the remaining bins—where the stellar light contributes more than 34% of the total flux—the derived stellar kinematics are robust, with uncertainties below 3%.

2.8. NIRSpec AGN PSF at 2.3 μm

From panel F of Figure 5, we derive the AGN light-fraction map as $1 - \gamma$, where γ denotes the stellar light fraction. The AGN light-distribution map, shown in the lower panel of Figure 6, is then obtained by multiplying this fraction map by the integrated-light map from the *JWST*/NIRSpec G235H/F170LP data cube. We parameterize the resulting AGN light distribution using a multi-Gaussian expansion (MGE; E. Emsellem et al. 1994), implemented with the `mge_fit_sector` routine from the MGEFit package (M. Cappellari 2002). The 2D AGN light distribution is expressed

Table 2. *JWST*/NIRSpec AGN MGE PSF model at 2.3 μm and *HST* Tiny Tim WFC3/F110W MGE PSF model

j	$(\text{Light fraction})_j$	σ_j (arcsec)	$\text{FWHM}_{\text{PSF}}^{\text{tot}}$ (arcsec)
(1)	(2)	(3)	(4)
<u>PSF_{AGN}</u>			
1	0.770	0.080	0.210
2	0.230	0.128	
<u>PSF_{HST}</u>			
1	0.442	0.028	
2	0.389	0.094	0.131
3	0.099	0.330	
4	0.070	0.825	

Notes. The first column gives the number of Gaussian components. The second column reports the light fraction of each Gaussian. The third column lists the Gaussian dispersions along the major axis. The fourth column lists the representative average FWHM of the *HST* photometric PSF, computed from their Gaussian components.

analytically as

$$\text{PSF}_{\text{AGN}}(r) = \sum_{j=1}^n \frac{F_j}{2\pi\sigma_j^2} \exp\left(-\frac{r^2}{2\sigma_j^2}\right),$$

where r is the radial coordinate, σ_j is the dispersion of Gaussian component j , and F_j is its normalized weight, with $\sum_{j=1}^n F_j = 1$. The best-fit MGE PSF model for the AGN light distribution comprises two Gaussians, which have an average FWHM of 0''.21, as listed in Table 2 and shown in the upper panel of Figure 6. This value is consistent with the STPSF synthetic *JWST*/NIRSpec PSF reported in Table 1 of D. D. Nguyen et al. (2025b) and with the empirical PSF derived by M. C. Bentz (2025) from observations of an isolated late-type star. We adopt this PSF model in this work to derive the black hole mass of M81 (Section 4.2).

3. IMAGING AND PHOTOMETRIC MODEL

Accurate dynamical modeling and M_{BH} measurements require a well-constrained estimate of the gravitational potential of the galaxy. We derived the stellar potential by scaling the galaxy's luminosity with a mass-to-light ratio (M/L). To model the stellar luminosity distribution with high fidelity, we combined high-resolution narrow-field space-based *HST* imaging with wide-field ground-based data from the 2MASS survey.

3.1. *HST* Observation and Its PSF Image

We modeled the stellar light distribution of M81 within a $110'' \times 110''$ field using *HST* imaging obtained on 24 June 2009 with the WFC3/IR channel, which has a pixel scale of 0''.09, and the broad-band F110W filter. The observation consists of a single exposure with a total on-source integration time of 143 seconds.

¹² <https://ned.ipac.caltech.edu>

¹³ v2.0.8: <https://pypi.org/project/pafit/>

¹⁴ <https://leda.univ-lyon1.fr/>

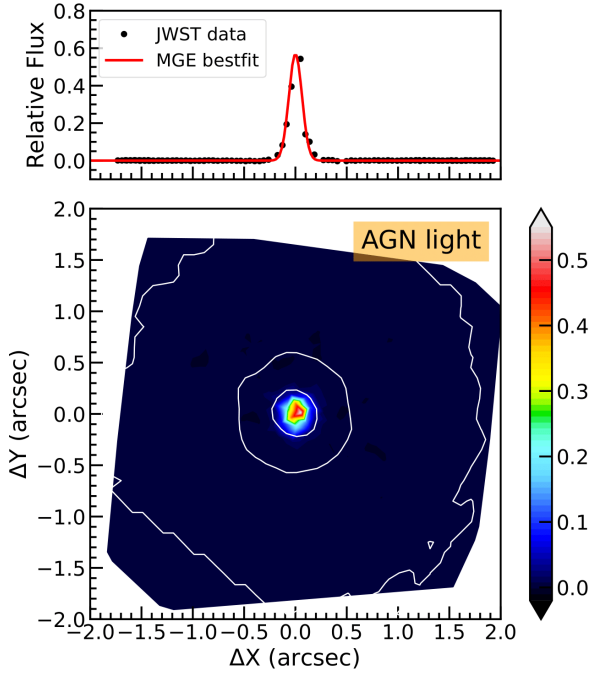


Figure 6. *Upper panel:* The 1D radial profiles of the spectrally extracted AGN signal from the *JWST*/NIRSpec G235H/F170LP data cube, shown together with the best-fitting MGE model of the PSF. The profile is constructed by mapping each data point to its projected radius, with negative and positive values corresponding to positions on opposite sides of the nucleus. *Lower panel:* The 2D image of the extracted AGN light distribution displayed on a logarithmic scale.

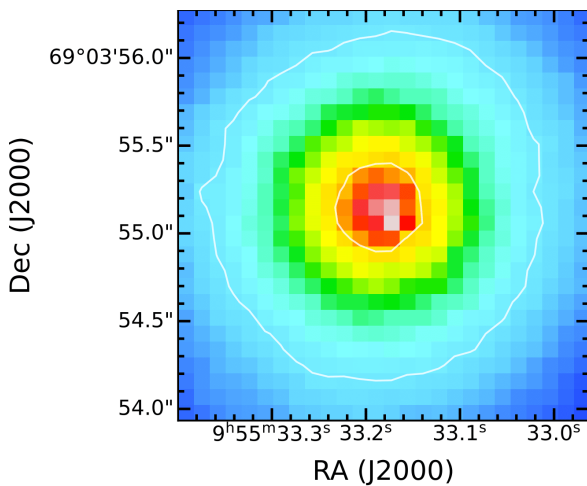


Figure 7. The central region of the *HST*/WFC3 F110W image reveals a peak in surface brightness that is offset by approximately $0.^{\prime}1$ to the southwest of the M81 nuclear centroid.

We required a PSF to deconvolve the *HST* image into the intrinsic stellar light distribution (Section 3.5). We generated a synthetic PSF using the *Tiny Tim* software package¹⁵ (J.

Table 3. Gaussian Parameters of the M81 MGE Model

j	$\lg \Sigma_{\star,j} (\mathrm{L}_\odot \mathrm{pc}^{-2})$	$\lg \sigma_j (\mathrm{arcsec})$	$q'_j (= b/a)$
(1)	(2)	(3)	(4)
1	5.511	-0.940	0.727
2	5.034	-0.468	0.900
3	4.873	-0.107	0.900
4	4.610	-0.194	0.900
5	4.172	0.543	0.681
6	4.280	0.569	0.900
7	4.007	1.020	0.550
8	3.630	1.112	0.843
9	3.234	1.374	0.621
10	3.207	1.516	0.717
11	3.070	1.754	0.766
12	2.783	2.078	0.500
13	2.353	2.391	0.500
14	1.497	2.468	0.900

Notes. The first column gives the number of Gaussian components. The second column reports the surface brightness of each Gaussian. The third column lists the Gaussian dispersions along the major axis. The fourth column provides the corresponding axial ratios.

Krist 1995; J. E. Krist et al. 2011), specifically employing the `tiny1` and `tiny2` routines, which simulate the PSF for a given filter, detector chip, chip position, and instrument configuration. To ensure consistency with the actual observations, the PSF was generated using the same exposure parameters as the *HST* image, and was subsequently convolved with an appropriate charge diffusion kernel to account for the redistribution of electrons into neighboring pixels on the detector.

3.2. 2MASS

To characterize the stellar light distribution of M81 beyond the central $110'' \times 110''$ region, we used a large-scale J-band image from the 2MASS survey, which covers a wavelength range of 1.12 – $1.36\mu\mathrm{m}$ and has a central wavelength of $1.235\mu\mathrm{m}$ (T. H. Jarrett et al. 2003). The 2MASS image has a pixel scale of $1''$ per pixel.

3.3. Center Offset in the *HST* F110W image?

We discovered that the peak brightness in the *HST* image appears to be offset $\sim 0.^{\prime}1$ southwest from the centroid of the M81 nucleus as seen in Figure 7. Given that we are observing this offset from the IR F110W image, it is unlikely that this feature is caused by dust extinction. The S/N in the *HST* image is high enough to verify that the AGN peak agrees well with the offset peak in the *HST* image. Thus, this offset could be the morphological evidence that the SMBH is not yet settled in the center. There are not many galaxies that are close enough for us to resolve such an offset between the SMBH’s location and the photometric center, except for the well-known example of M31 nucleus (T. R. Lauer et al. 2005)

¹⁵ <https://github.com/spacetelescope/tinytim>

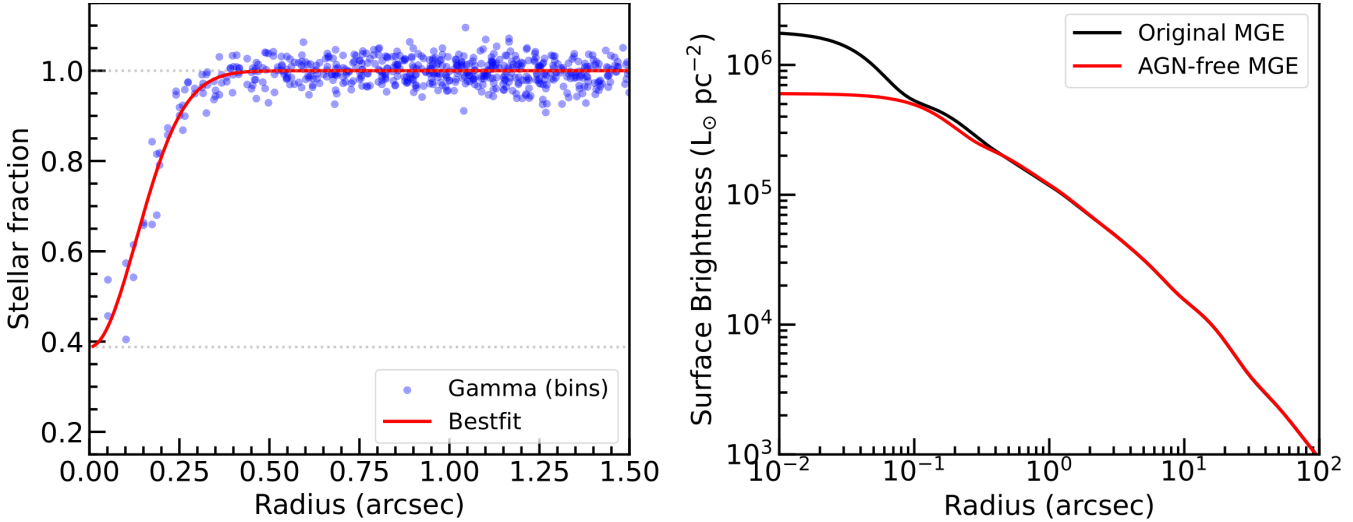


Figure 8. *Left:* The stellar light fraction distribution for all kinematic bins measured in Section 2.7 and extracted from panel F of Figure 5. The red curve represents the best-fit profile, which dominates beyond $0.^{\prime}3$ but declines sharply toward the galaxy center. *Right:* Comparison between the scaled *HST* radial profile (black line) and the profile constrained by the stellar contribution (red line) measured spectroscopically with *JWST/NIRSpec* G235H/F170LP.

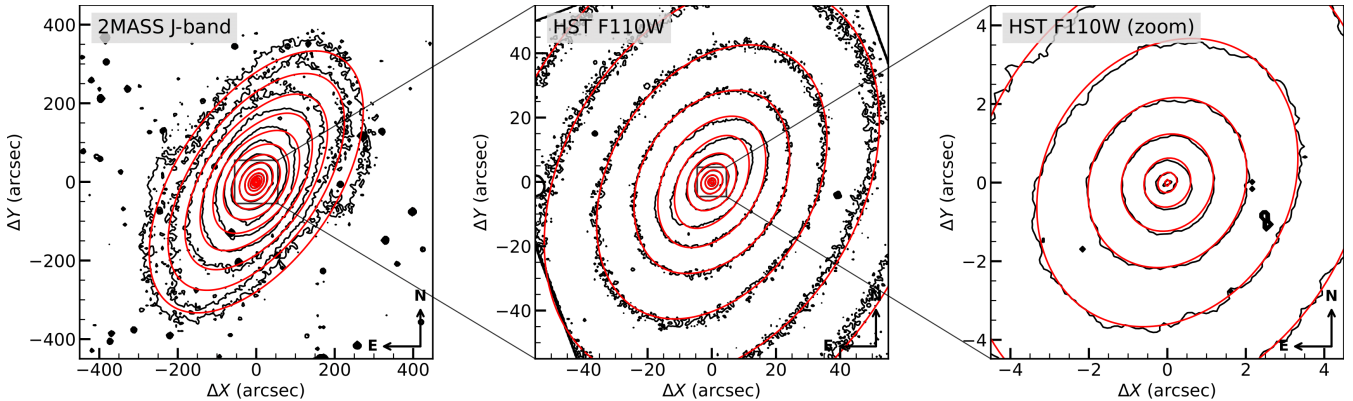


Figure 9. *Left:* Isophotes of M81 from the 2MASS J-band image (black contours) and the corresponding MGE model (red contours) are shown over a $1000'' \times 1000''$ FoV. *Middle:* The same comparison is presented for the *HST/WFC3/IR* F110W image, covering a $110'' \times 110''$ FoV. *Right:* Zoom-in of the central $10'' \times 10''$ region of the *HST* image. The MGE model accurately reproduces the observed isophotes across all spatial scales. Contours represent decreasing surface brightness levels, with a spacing of $1 \text{ mag arcsec}^{-2}$.

and the recent same discovery in the nucleus of NGC 4486B at the Virgo cluster (B. Tahmasebzadeh et al. 2025).

Spatial or kinematic offsets between the location of the SMBH and the photometric or dynamical center of a galaxy have been reported in several nearby systems and interpreted in a variety of contexts. A classic example is the double nucleus of M31, in which the brighter off-center component (P1) and the true nucleus (P2) can be understood as asymmetric stellar structures in an eccentric disk around the central BH (T. R. Lauer et al. 2005), and measurements indicate a small displacement of the SMBH from the bulge center consistent with this model (e.g., T. R. Lauer et al. 1998; J. Kormendy & R. Bender 1999). Similarly, early *HST* studies suggested a projected offset of $\sim 0.^{\prime}1$ in M87 between the nuclear point source and the galaxy photocenter, though sub-

sequent work attributed much of this apparent displacement to temporal jet variability rather than a true SMBH displacement (e.g., D. Batcheldor et al. 2010). Searches for recoiling or displaced SMBHs in samples of nearby early-type galaxies have also found modest ($\lesssim 10$ pc) AGN-photocenter separations in a fraction of objects, which can be explained by post-merger recoil oscillations or asymmetric jet acceleration (e.g., D. Lena et al. 2014). Observations of velocity-offset AGN emission lines further suggest that kinematic displacements in ionized gas can arise from outflows, dual nuclei, or eccentric nuclear structures (e.g., F. Müller-Sánchez et al. 2016). More recent cosmological simulations indicate that off-center SMBHs, particularly in brightest cluster galaxies, may be common outcomes of hierarchical assembly, with roughly one third of systems showing significant displace-

ments at $z = 0$ due to merger dynamics (e.g., [Q. Chu et al. 2022](#)). These studies together demonstrate that while exact SMBH–galaxy center coincidence is the norm, small offsets do occur and can provide clues to recent dynamical history beyond simple noise or measurement uncertainty.

3.4. Separating Central AGN Emission from Stellar Light in HST image

Our galaxy mass model of M81 must represent the stellar light distribution only, free from contamination by the central AGN. To achieve this, we corrected the *HST*/WFC3 IR F110W image by modeling and subtracting the AGN point source before fitting the MGE. Following the approach of [D. A. Simon et al. \(2024\)](#), we estimated the AGN’s spatial profile from the NIRSpec stellar fraction map (γ ; panel F of Figure 5), assuming minor differences between the *HST*/WFC3 IR F110W and *JWST*/NIRSpec G325H/F170LP PSFs are negligible. The fractional contribution of the AGN at a given radius is $(1 - \gamma)$. We modeled this radial profile by assuming the AGN light distribution can be approximated by a Gaussian function, which leads the purely stellar contribution to the form:

$$\gamma(r) = 1 - \Delta\gamma \cdot \exp\left(-\frac{r^2}{2\sigma^2}\right),$$

where the best fit values are $\Delta\gamma = 0.612$ and $\sigma = 0''.131$ (left panel of Figure 8). Using this fit, we constructed a modified (i.e., AGN-free) *HST*/WFC3 IR F110W image in which the innermost sub-arcsecond region was replaced with the AGN-free stellar image. The fitted profile was then matched to the original *HST*/WFC3 IR F110W surface brightness profile (i.e., AGN + stars) beyond $0''.3$ (right panel of Figure 8).

3.5. Full Surface Brightness Profile and Galaxy Mass Model of M81

Before constructing the 2D stellar surface-brightness distribution of M81, we estimated and subtracted the sky background for the *HST*/WFC3 IR F110W and 2MASS *J*-band images independently. For each image, the sky level was determined as the median signal measured within several 10×10 pixel² boxes placed in source-free regions at projected distances greater than $40''$ (for the *HST*/WFC3 image) and $400''$ (for the 2MASS image) from the galaxy center. These median values were then subtracted from the corresponding images to produce sky-subtracted frames used in the subsequent analysis. Regions affected by dust obscuration and foreground stars were masked in both the *HST*/WFC3 IR F110W and 2MASS *J*-band images before the fitting procedure.

We then constructed the 2D stellar surface-brightness distribution of M81 using the `mge_fit_sectors_regularized` routine from the MGEFit package (see footnote 15), fitting the sky-subtracted *HST*/WFC3 IR F110W and 2MASS *J*-band images simultaneously. During the fitting process, we accounted for the *HST*/WFC3 IR F110W PSF to recover the

galaxy’s intrinsic light distribution. Specifically, the PSF image was first modeled as an MGE, whose parameters are listed in Table 2, with a FWHM of $0''.131$, which was then convolved with the *HST*/WFC3 IR F110W image during the fit. This step is essential, as the accuracy of the M_{BH} measurement depends critically on how well the central stellar mass distribution is modeled.

The procedure consisted of the following steps:

- We extracted multi-sector surface-brightness profiles from the sky-subtracted *HST*/F110W image (describing the inner regions) and from the sky-subtracted 2MASS *J*-band image (describing the outer regions). The central region of the sky-subtracted 2MASS image overlapping with the *HST* FoV was masked to avoid double-counting and to prevent the lower-resolution data from influencing the inner profile.
- We placed the two datasets on a consistent photometric scale. We used the `PhotometryMatch` routine to determine the relative flux offset and multiplicative flux scaling factor between the sky-subtracted *HST* and 2MASS profiles. These parameters were derived by minimizing photometric residuals in an overlap annulus between $5''$ and $50''$, where both datasets have a reliable signal. This step accounts for differences in pixel scale, absolute calibration, and background subtraction between the two images.
- We combined the sky-subtracted *HST* radial photometry at radii $r < 50''$ with the sky-subtracted 2MASS photometry at $r > 50''$ into a single, continuous surface-brightness profile.
- We then applied the MGE fit to this combined profile, with PSF convolution applied only to the *HST* component. The resulting MGE therefore represents a joint fit to the inner high-resolution *HST* data and the outer wide-field 2MASS data, ensuring a smooth and physically consistent stellar mass model across all radii.

Next, the flux unit of counts/second was converted to physical units of $\text{L}_{\odot} \text{ pc}^{-2}$ following the procedure outlined by [D. Thatte et al. \(2009\)](#), adopting photometric zero-points and absolute magnitudes for the Sun in the Vega system ([C. N. A. Willmer 2018](#)). For the *HST* image, we used $m_{0,\text{F110W}} = 26.05 \text{ mag}$ ¹⁶ and $M_{\text{Vega,F110W}} = 3.79 \text{ mag}$; for the 2MASS image, $m_{0,\text{J}} = 20.92 \text{ mag}$ and $M_{\text{Vega,J}} = 3.67 \text{ mag}$ were adopted. Galactic extinction corrections of $A_{\text{F110W}} = 0.071 \text{ mag}$ for the *HST* image ([E. F. Schlafly & D. P. Finkbeiner](#)

¹⁶ https://www.stsci.edu/files/live/sites/www/files/home/hst/instrumentation/wfc3/documentation/instrument-science-reports-isrs/_documents/2024/WFC3-ISR-2024-13.pdf

2011) and $A_J = 0.058$ mag¹⁷ for the 2MASS image were also applied.

Both the original and modified *HST* images were then fitted with MGE models, which were subsequently matched to the 2MASS J -band MGE model at large radii. We list in Table 3 this combined and AGN-free MGE model, which consists of 14 concentric Gaussian components and has a somewhat flatter central profile (red line) compared to the AGN-contaminated one (black line), as seen in the right panel of Figure 8. It is clear that the AGN-contaminated stellar light near the nucleus is non-negligible and, if uncorrected, would significantly bias the SMBH mass measurement for M81. Figure 9 presents this best-fitting, combined, and AGN-free MGE model overlaid on the observed surface brightness distribution of M81, based on the 2MASS J -band image (left) and the *HST* WFC3/IR F110W image (middle). A zoom-in of the central $10'' \times 10''$ region from the *HST* WFC3/IR F110W image is shown in the right panel. This figure demonstrates that the combined MGE model accurately reproduces the galaxy's isophotes across a broad range of spatial scales, confirming its suitability for subsequent dynamical modeling.

In the subsequent dynamical analysis of M81, we adopted this best-fitting, combined, and AGN-free MGE model as the fiducial stellar-mass model, while the similar best-fitting and combined but AGN-contaminated MGE model was used to assess the systematic uncertainties.

The 2D light distribution is then deprojected, assuming an axisymmetric potential and a free inclination angle (i), to yield a 3D axisymmetric luminosity profile. By multiplying this luminosity distribution by the M/L_J ratio in the J band, we obtain a model of the mass density, from which the gravitational potential can be calculated via the Poisson equation.

4. DYNAMICAL MODELLING

4.1. Jeans Anisotropic Models

We used both the cylindrically aligned JAM models (JAM_{cyl}; M. Cappellari 2008) and the spherically aligned version (JAM_{sph}; M. Cappellari 2020), each assuming an axisymmetric potential, to assess how velocity-ellipsoid alignment affects the dynamical M_{BH} determination in M81 by comparing the observed NIRSpec G235H/F170LP V_{rms} map with model predictions.

The JAM_{cyl} model aligns the velocity ellipsoid with cylindrical coordinates (R, ϕ, z). The anisotropy is described by $\beta_z = 1 - (\sigma_z/\sigma_R)^2$. In contrast, the JAM_{sph} model aligns the velocity ellipsoid with spherical coordinates (r, θ, ϕ). Here, the anisotropy is quantified by $\beta_r = 1 - (\sigma_r/\sigma_\theta)^2$. In both models, all three components of the velocity ellipsoid are allowed to be different.

¹⁷ <https://irsa.ipac.caltech.edu/applications/DUST/>

We constructed our models using the `jam.axi.proj` routine in JAMPy¹⁸ (M. Cappellari 2020), setting `align='cyl'` for cylindrical alignment and `align='sph'` for spherical alignment to compute the LOSVD moments $\langle V_{\text{los}}^2 \rangle$.

4.2. Model Grid and Parameter Space

Both JAM_{cyl} and JAM_{sph} estimate M_{BH} (sampled logarithmically) and additional parameters sampled linearly, including the mass-to-light ratio (M/L_J) and the orbital anisotropy. In JAM_{sph}, the radial anisotropy (β_r) is parameterized as the ratio σ_θ/σ_r , whereas in JAM_{cyl}, the vertical anisotropy (β_z) is defined as the ratio σ_z/σ_R . In the JAM_{cyl} models, we adopted a constant anisotropy with no imposed priors. For the physically motivated JAM_{sph} models, we implemented the D. A. Simon et al. (2024) logistic anisotropy prescription with the priors described in Section 4.4. For the inclination parameter (i , converted to q_{min}), we fixed it to the photometrically determined value of $i \approx 63^\circ$ ($q_{\text{min}} \approx 0.05$), as M81 is a spiral galaxy with a relatively low and well-constrained inclination inferred from its dust-lane morphology. Allowing for near edge-on configurations is clearly inconsistent with the observed photometry and was therefore not considered. The adopted inclination is taken from the HyperLEDA database¹⁹.

In these JAMs, we accounted for the effects of the NIRSpec G235H/F170LP PSF at $2.3 \mu\text{m}$, testing both synthetic and empirical PSFs. D. D. Nguyen et al. (2025b) showed that synthetic PSF 1 (FWHM_{PSF}^{tot} = $0''.08$) and PSF 2 (FWHM_{PSF}^{tot} = $0''.15$) provide good fits to the JWST/NIRSpec stellar kinematics of NGC 4258, while PSF 3 (FWHM_{PSF}^{tot} = $0''.20$) underestimates the central V_{rms} by $\approx 20 \text{ km s}^{-1}$. We also tested empirical NIRSpec IFU PSFs constrained by F. D'Eugenio et al. (2024, 2025), which are consistent with our PSF 2, whereas those reported by M. C. Bentz (2025) and our AGN-based PSF derivation in Section 2.8 are both consistent with our synthetic PSF 3. In addition, we explored both constant and radially varying M/L_J assumptions (Section 4.3) to assess systematic uncertainties in the M_{BH} measurement of M81.

In total, we performed 12 JAM model runs as listed in Table 4 and summarized below, which together bracket the main sources of systematic uncertainty in our dynamical analysis:

1. **Anisotropy alignment (2 options):** Either cylindrically aligned velocity ellipsoid (JAM_{cyl}) or spherically aligned one (JAM_{sph}).
2. **Point Spread Function (3 options):** Three STPSF (M. Perrin et al. 2025) synthetic JWST/NIRSpec PSFs were tested (Table 1 of D. D. Nguyen et al. 2025b).

¹⁸ v7.2.0: <https://pypi.org/project/jampy/>

¹⁹ <http://atlas.obs-hp.fr/hyperleda/>

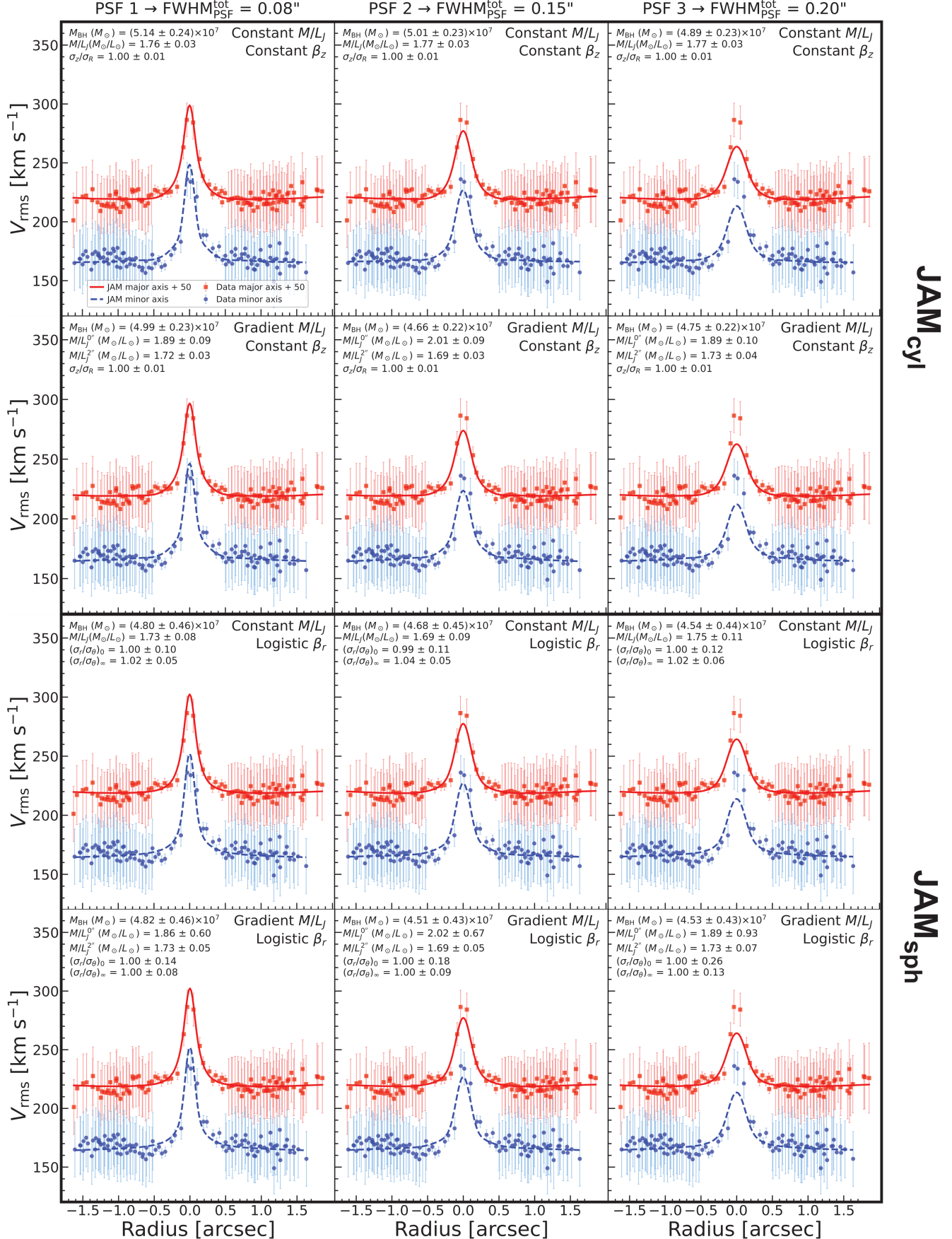


Figure 10. Stellar kinematics extracted from the NIRSpec G235H/F170LP data cube of M81 are shown as filled red (major axis + 50 km s^{-1}) and blue (minor axis) points, overlaid with best-fit JAM models assuming various combinations of M/L_j and orbital anisotropy. Each model includes its corresponding best-fit parameters and associated 1σ uncertainties in the legend.

3. Mass-to-light ratio (2 options): Either a constant M/L_J or a radially varying M/L_J within the NIRSpec FoV data cube (Section 4.3).

4.3. Linearly Varying M/L_J Profile

Possible population variation within the nucleus of M81 can bias both the central M/L_J and M_{BH} measurements. We performed an additional test, in which the M/L_J values beyond the NIRSpec FoV ($r > 2''$) were fixed to the best-fit value obtained from the corresponding models with a constant M/L_J parameter. However, within $2''$, M/L_J was allowed to vary linearly toward a central value $M/L_J^{0''}$.

In JAMs, the $M/L_J(r)$ profile is implemented by associating a different $(M/L_J)_j$ to each Gaussian component with dispersion σ_j in the MGE listed in Table 3, as follows:

$$\left(\frac{M}{L_J}\right)_j = \begin{cases} M/L_J^{0''} + \frac{M/L_J^{2''} - M/L_J^{0''}}{2''} \times \sigma_j, & \sigma_j < 2'' \\ M/L_J^{2''}, & \sigma_j \geq 2'' \end{cases} \quad (1)$$

4.4. Logistic Anisotropy for JAM_{sph} Models

While formally Jeans models are subject to the mass-anisotropy degeneracy (J. Binney & G. A. Mamon 1982), our understanding of galaxy dynamics has vastly improved since then. It now allows us to place physically motivated priors on the stellar orbital structure, significantly improving the reliability of the mass measurement. Both observations and simulations of massive galaxies consistently show a characteristic anisotropy profile: orbits are nearly isotropic or mildly radially-biased at large radii, but become tangentially-biased inside the BH's SOI. This orbital structure is thought to be a natural outcome of SMBH binary scouring during galaxy mergers, which preferentially ejects stars on radial orbits (e.g., M. Milosavljević & D. Merritt 2001; A. Rantala et al. 2024). While this scenario has been primarily studied in massive elliptical galaxies, the lack of radially-biased orbits near the BH has also been observed in lower-mass fast-rotating systems (see a review of the observations in, M. Cappellari 2026, Figure 10).

To capture this expected behavior, we explored the JAM_{sph} model with a flexible, radially varying anisotropy, as done by D. A. Simon et al. (2024). This model uses a logistic function of $\log r$ to describe the radial anisotropy profile $\beta_r(r) = 1 - \sigma_r^2/\sigma_r^2$:

$$\beta_r(r) = \beta_{r,0} + \frac{\beta_{r,\infty} - \beta_{r,0}}{1 + (r_a/r)^\alpha} \quad (2)$$

Here, $\beta_{r,0}$ and $\beta_{r,\infty}$ are the anisotropy values at the center and at large radii, respectively, and r_a is the transition radius. We re-express the anisotropy in terms of the more intuitive velocity dispersion ratio $\sigma_r/\sigma_\theta = 1/\sqrt{1 - \beta_r}$.

Based on the established physics, we applied specific priors to constrain the model parameters. This approach was successfully tested on two benchmark galaxies with very accurate, independent M_{BH} determinations: the massive elliptical galaxy M87 (D. A. Simon et al. 2024) and the spiral galaxy NGC 4258 (D. D. Nguyen et al. 2025b), which has a morphology similar to M81. In both cases, the JAM models with these physically-motivated priors recovered the known BH masses, validating the reliability of this method.

Following this validated approach, we restricted the inner anisotropy to be tangentially biased or isotropic ($0.5 < (\sigma_r/\sigma_\theta)_0 < 1$) and the outer anisotropy to be isotropic or mildly radially biased ($1 < (\sigma_r/\sigma_\theta)_\infty < 1.3$). The anisotropy transition radius was fixed at $r_a = 0''.55$, slightly larger than the SMBH's SOI ($r_{\text{SOI}} \approx 0''.5$; see Section 5.1), to ensure the model can capture the expected transition from a tangentially-biased inner region to a more isotropic outer region. Finally, we fixed the sharpness parameter to $\alpha = 2$ to reduce the dimensionality of the parameter space and minimize degeneracies.

4.5. MCMC Fitting and Uncertainty Estimation

We ran the JAM models within a Markov chain Monte Carlo (MCMC) framework to explore the full parameter space. Sampling was performed using the adaptive Metropolis algorithm (H. Haario et al. 2001), as implemented in the ADAMET²⁰ package (M. Cappellari et al. 2013). Each MCMC chain comprised 5×10^4 steps, with the first 20% of samples discarded as burn-in. The remaining samples were used to construct posterior probability distributions. The most likely values for the model parameters were identified as those corresponding to the maximum likelihood, and uncertainties were estimated from the 1σ (16th–84th percentile) and 3σ (0.14th–99.86th percentile) confidence intervals (CLs).

Dynamical modeling of our numerous high-precision NIRSpec kinematic data points presents two challenges:

- Underestimated Uncertainties:** The formal statistical errors on derived parameters can become unrealistically small due to the unmodelled systematic effects.
- Dominance of Large-Radii Data:** The χ^2 statistic can be disproportionately influenced by the large number of data points at large radii. This risks biasing the M_{BH} measurement, which should be dictated primarily by the kinematics within the BH's SOI.

To mitigate the first issue, we adopt an error inflation scheme. We base our approach on the heuristic $\Delta\chi^2$ -increase method of R. C. E. van den Bosch & G. van de Ven (2009), which, in a Bayesian framework, is equivalent to inflating

²⁰ v2.0.9: <https://pypi.org/project/adamet/>

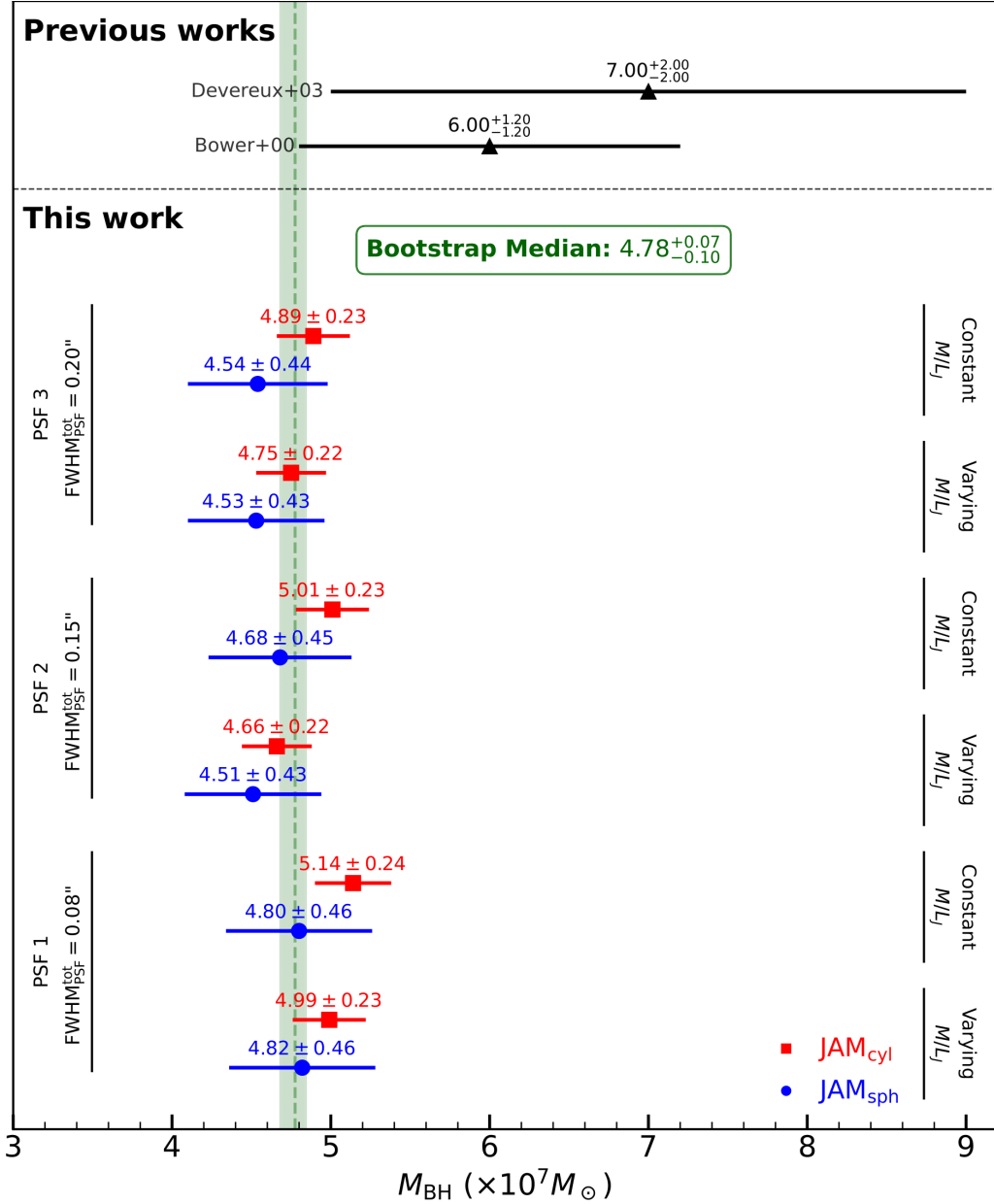


Figure 11. Black hole mass measurements for M81 from 12 conventional JAM models applied to the NIRSpec G235H/F170LP data cube. Individual measurements and their 1σ uncertainties reflect variations in PSF, orbital anisotropy, and stellar M/L_J assumptions. Vertical dashed lines mark the adopted M_{BH} , with shaded regions indicating the ensemble median and 68% bootstrap confidence interval. For comparison, previous estimates from G. A. Bower et al. (2000) and N. Devereux et al. (2003) are shown; these earlier values relied on restrictive stellar dynamical assumptions or disturbed ionized gas kinematics. The present analysis provides the most reliable measurement of M_{BH} in M81 to date.

the kinematic measurement errors by a factor of $(2N)^{1/4}$, where N is the number of data points (M. Mitzkus et al. 2017, Section 6.1). While this technique is now standard for ALMA-based M_{BH} measurements (e.g., D. D. Nguyen et al. 2020; M. D. Smith et al. 2019, 2021; E. V. North et al. 2019), a uniform inflation across all radii does not resolve the second challenge.

Therefore, we apply the inflation selectively. We preserve the formal kinematic uncertainties for all data points inside

the SOI ($r \leq r_{\text{SOI}} \approx 0.5''$), where the SMBH's gravitational potential dominates. For the $N_{r > r_{\text{SOI}}} = 620$ kinematic bins outside this radius, we inflate their associated errors by a factor of $(2N_{r > r_{\text{SOI}}})^{1/4}$. This refined strategy ensures the M_{BH} determination is driven by the central kinematics while still accounting for potential systematic errors at larger radii. This selective approach has been successfully employed in previous dynamical studies using integral-field data from Gemini/NIFS (D. A. Drehmer et al. 2015), VLT/MUSE (S. Thater

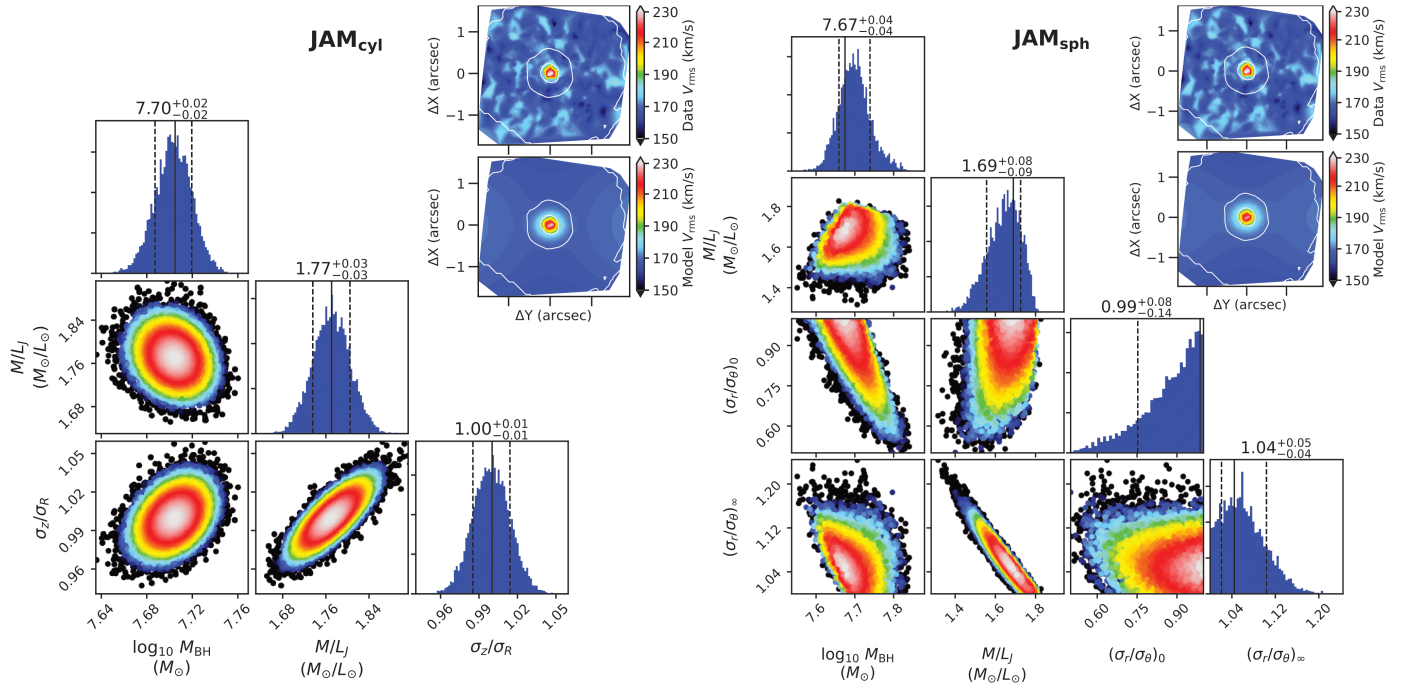


Figure 12. *Left:* Posterior distributions for the JAM_{cyl} model with constant M/L_J and anisotropy, obtained following the burn-in phase of the ADAMET MCMC optimization, are presented for the nuclear stellar kinematics of M81 using the NIRSpec G235H/F170LP data. The resulting triangle plot displays the 2D projected probability distributions of the model parameters (M_{BH} , M/L_J , σ_z/σ_R), with 1D marginalized histograms shown along the diagonal. Solid vertical lines indicate the best-fit values, while dashed lines denote the 1σ uncertainties. Inset panels in the upper right compare the observed and model-predicted V_{rms} on a consistent velocity scale. The observed V_{rms} map was symmetrized under the assumption of axisymmetry using the SYMMETRIZE_VELFIELD routine from the PLOTBIN^a package. Both the symmetrized data and model prediction were visualized with PLOT_VELFIELD. The strong agreement across the NIRSpec FoV demonstrates the high fidelity of the model. *Right:* Same as the left panel, but applied the JAM_{sph} models with logistic varying β_r profile and the model parameters (M_{BH} , M/L_J , $(\sigma_r/\sigma_\theta)_0$, $(\sigma_r/\sigma_\theta)_\infty$).

^av3.1.7: <https://pypi.org/project/plotbin/>

et al. 2022, Section 4.3), and recently *JWST*/NIRSpec (D. D. Nguyen et al. 2025b).

5. RESULTS AND DISCUSSION

5.1. Dynamical Supermassive Black Hole Mass Constraints

We summarize in Table 4 the best-fit parameters and their 1σ uncertainties for the 12 conventional JAM models used to fit the NIRSpec G235H/F170LP V_{rms} data. Across all model assumptions, the inferred M_{BH} ranges from $(4.51\text{--}5.14) \times 10^7 M_\odot$, and the M/L_J values span $(1.69\text{--}2.02) M_\odot/L_\odot$. While both M_{BH} and M/L_J are relatively insensitive to the choice of PSF, they are more strongly affected by the assumed velocity ellipsoid alignment. Specifically, the JAM_{cyl} models yield M_{BH} and M/L_J values that are $\approx 7\%$ higher than those from the JAM_{sph} models.

Figure 10 shows the V_{rms} profiles for all 12 best-fitting JAM models (with their 1σ uncertainties), extracted along the major and minor axes of M81. These are directly compared to the observed V_{rms} profiles from the NIRSpec G235H/F170LP data, extracted in the same manner. Overall, all models provide a good match to both the data and to each other across

the NIRSpec FoV, despite differences in the assumed M/L_J profiles and orbital anisotropy.

A systematic offset is observed between the models and the data in the innermost kinematic bins, which is likely attributable to uncertainties in the NIRSpec PSF modeling. To investigate this, we tested three synthetic PSFs from D. D. Nguyen et al. (2025b) with different widths. The models using the broadest PSF (PSF 3, $\text{FWHM}_{\text{PSF}}^{\text{tot}} \approx 0''.2$), consistently underpredict the central V_{rms} by $\approx 20 \text{ km s}^{-1}$ (right column of Figure 10). Conversely, models with the narrowest PSF (PSF 1, $\text{FWHM}_{\text{PSF}}^{\text{tot}} \approx 0''.08$) tend to overpredict the central V_{rms} by $\approx 15 \text{ km s}^{-1}$ (left column). The models providing the best match to the data, including the innermost bins, are those using the intermediate PSF 2 ($\text{FWHM}_{\text{PSF}}^{\text{tot}} \approx 0''.15$; middle column). This preference for the $\approx 0''.15$ PSF is consistent with the findings for NGC 4258 in D. D. Nguyen et al. (2025b), giving us confidence that our models are using a realistic representation of the instrumental resolution.

Notably, our derived M_{BH} value is 17% lower than that inferred from the VLT/GMOS IFU velocity dispersion and the K. Göltekin et al. (2009) $M_{\text{BH}}-\sigma$ relation, while it is 31.7% lower than the gas-based M_{BH} measurement from *HST*/STIS

Table 4. Summary of the 12 JAM models best-fitting parameters and *formal* uncertainties.

M/L_J	FWHM _{PSF} ^{tot} (")	M_{BH} ($\times 10^7 M_{\odot}$)	M/L_J	$M/L_J^{0''}$ (M_{\odot}/L_{\odot})	$M/L_J^{2''}$ (M_{\odot}/L_{\odot})	σ_z/σ_R	$(\sigma_r/\sigma_{\theta})_0$	$(\sigma_r/\sigma_{\theta})_{\infty}$
(1)	(2)	(3)	(4)	(5)	(6)	(7)	(8)	(9)
JAM _{cyl} models with constant anisotropy								
Constant	0.08	5.14 ± 0.24	1.76 ± 0.03	1.00 ± 0.01
Constant	0.15	5.01 ± 0.23	1.77 ± 0.03	1.00 ± 0.01
Constant	0.20	4.89 ± 0.23	1.77 ± 0.03	1.00 ± 0.01
Varying	0.08	4.99 ± 0.23	...	1.89 ± 0.09	1.72 ± 0.03	1.00 ± 0.01
Varying	0.15	4.66 ± 0.22	...	2.01 ± 0.09	1.69 ± 0.03	1.00 ± 0.01
Varying	0.20	4.75 ± 0.22	...	1.89 ± 0.10	1.73 ± 0.04	1.00 ± 0.01
JAM _{sph} models with radially-varying logistic anisotropy								
Constant	0.08	4.80 ± 0.46	1.73 ± 0.08	1.00 ± 0.10	1.02 ± 0.05
Constant	0.15	4.68 ± 0.45	1.69 ± 0.09	0.99 ± 0.11	1.04 ± 0.05
Constant	0.20	4.54 ± 0.44	1.75 ± 0.11	1.00 ± 0.12	1.02 ± 0.06
Varying	0.08	4.82 ± 0.46	...	1.86 ± 0.60	1.73 ± 0.05	...	1.00 ± 0.14	1.00 ± 0.08
Varying	0.15	4.51 ± 0.43	...	2.02 ± 0.67	1.69 ± 0.05	...	1.00 ± 0.18	1.00 ± 0.09
Varying	0.20	4.53 ± 0.43	...	1.89 ± 0.93	1.73 ± 0.07	...	1.00 ± 0.26	1.00 ± 0.13

Note: Column (1): Assumed M/L_J profile type. Column (2): Total FWHM of the synthetic PSF model. Column (3): Best-fit black hole mass. Column (4): Best-fit constant M/L_J . Columns (5) and (6): Best-fit central and outer M/L_J for the varying profile. Column (7): Best-fit vertical anisotropy for JAM_{cyl} models. Column (8): Best-fit central radial anisotropy for JAM_{sph} models. Column (9): Best-fit outer radial anisotropy for JAM_{sph} models.

(N. Devereux et al. 2003) and 26.5% lower than the widely adopted value from J. Kormendy & L. C. Ho (2013). More specifically, the derived M_{BH} values are insensitive to the assumed alignment of the velocity ellipsoid but are sensitive to the adopted M/L_J profile in the nucleus of M81.

In contrast, the orbital anisotropy of the nuclear stellar motions in M81 is well constrained and does not depend on whether a constant or varying M/L_J is assumed. The best-fit JAM_{cyl} models indicate nearly isotropic kinematics, with $\sigma_z/\sigma_R \sim 1$ (i.e., $\beta_z \sim 0$). For the JAM_{sph} models, we adopt a fixed transition radius $r_a = 0''.55$ (see Section 4.4). The best-fit models indicate that the ratio of stellar velocity dispersions (σ_r/σ_{θ}) at the center varies from ~ 0.55 to ~ 1.0 depending on the adopted PSF model (i.e., $\beta_r < 0$) and suggesting a slightly tangential bias. Beyond r_a , the orbits transition to a radially biased structure with $(\sigma_r/\sigma_{\theta})_{\infty} \sim 1.20$ (i.e., $\beta_r > 0$).

Figure 11 shows our 12 M_{BH} measurements and their 1σ uncertainties, providing a presentation-ready summary of the most precise M_{BH} constraint for M81 based on the spatially resolved NIRSpec G235H/F170LP IFU stellar kinematics. Following the approach of D. D. Nguyen et al. (2025b), we derive robust SMBH estimates from the 12 conventional JAM models by adopting the medians and their 68% (1σ) bootstrap confidence intervals, yielding $M_{\text{BH}} = (4.78^{+0.07}_{-0.10}) \times 10^7 M_{\odot}$.

Figure 12 shows example 2D posterior distributions for the JAM_{cyl} model with constant anisotropy (left) and the JAM_{sph} model with logistic anisotropy (Eq. 2; right). Both models assume a constant M/L_J within the NIRSpec FoV and PSF 2.

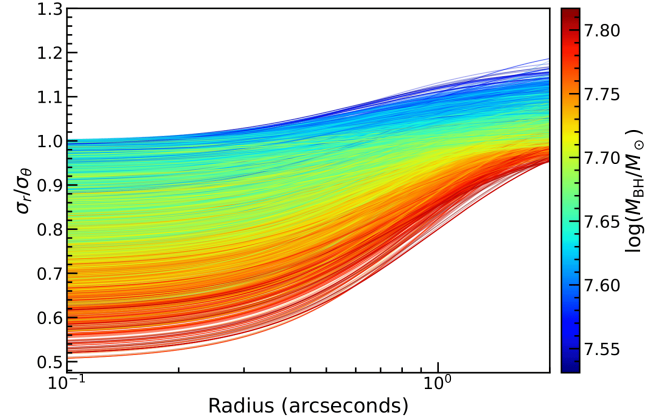


Figure 13. Plot of 10,000 anisotropy profiles randomly sampled from the MCMC chain of the JAM_{sph} with logistic anisotropy Figure 12, color-coded by their corresponding M_{BH} values. The profiles show clear evidence of a radially increasing anisotropy ratio and strongly exhibit the black hole mass–anisotropy degeneracy like M87 (D. A. Simon et al. 2024) and NGC 4258 (D. D. Nguyen et al. 2025b). The orbital anisotropy varies with black hole mass: stars orbiting more massive black holes exhibit tangentially biased motions, whereas those around smaller black holes show radial anisotropy.

Point colors indicate relative likelihood, with white corresponding to the maximum likelihood and the 1σ confidence level (CL) region, and black marking the 3σ CL. The accompanying 1D histograms along the diagonal are used to determine the best-fit values and 1σ uncertainties, which incorporate the propagation of stellar kinematics and statistical

errors. The figure also demonstrates the close agreement between the observed V_{rms} and the predictions from the best-fit JAM_{cyl} and JAM_{sph} models at the upper right corner of each triangle, assuming the major axes are aligned horizontally, with relative errors less than 5% in each case.

In the best-fitting JAM_{cyl} model, the remaining two parameters are well constrained, whereas in the best-fitting JAM_{sph} model, only the M_{BH} and M/L_J parameters are well constrained. The other parameters of the logistic anisotropy are limited by their priors to enforce physically plausible stellar orbits around the SMBH and within the NIRSpec FoV.

Across all JAM models, there is no significant covariance between M_{BH} and M/L_J within the 3σ CLs, indicating that both parameters are well constrained. In the JAM_{cyl} model, M_{BH} and M/L_J each show positive covariance with the orbital anisotropy parameter (σ_z/σ_R), whereas in the JAM_{sph} model, these covariances are negative with respect to (σ_θ/σ_r). This contrast highlights the complexity of how variations in M_{BH} or M/L_J can compensate for changes in anisotropy during the fitting process.

Our stellar-based M_{BH} measurements, derived under both cylindrical and spherical velocity ellipsoid assumptions, yield $r_{\text{SOI}} \approx 0''.5$ (or 9 pc), estimated using the method described in Section 1. These values are 5 times larger than the *JWST* spatial resolution, indicating that the M_{BH} determinations are robust and spatially well resolved. The dynamical influence of the SMBH is clearly detected within the central ≈ 80 spaxels in area.

5.2. The Mass–Anisotropy Degeneracy

A well-known characteristic of Jeans modeling is the mass-anisotropy degeneracy, where a given kinematic profile can be fit by different combinations of mass and orbital anisotropy. This effect is clearly illustrated in Figure 13, which shows 10,000 anisotropy profiles randomly drawn from the posterior distribution of our logistic JAM_{sph} model. The figure shows the expected covariance between M_{BH} and the anisotropy profile: higher M_{BH} values are required to fit the data when the stellar orbits are more tangentially biased, while lower M_{BH} values are consistent with more radial orbits. This behavior is not a flaw in our approach but an inherent property of stellar dynamics, and it has been observed in similar analyses of other galaxies like NGC 4258 (Figure 9 of D. D. Nguyen et al. 2025b) and M87 (Figure 15 of D. A. Simon et al. 2024).

What is crucial for a reliable mass measurement is that this degeneracy is properly sampled and accounted for in the final uncertainty budget. Our Bayesian MCMC framework is designed to do precisely this. By exploring the full parameter space, the sampler covers all degenerate solutions consistent with the data and our physically motivated priors. The final posterior probability distribution for M_{BH} is marginalized over all other parameters, including the full range of

allowed anisotropy profiles. Therefore, the reported CLs on our M_{BH} measurement robustly incorporate the uncertainty arising from the mass-anisotropy degeneracy.

5.3. Additional Uncertainty Budgets

5.3.1. Distances

Unlike most galaxies, the distance to M81 is exceptionally well-determined. As stated in the Introduction, we adopt a distance of $D = 3.63 \pm 0.14$ Mpc, which is the mean of five high-quality determinations based on the Cepheid and Tip of the Red Giant Branch methods. This precision is corroborated by the NASA/IPAC NED, which lists 99 distance determinations, yielding a formal average of 3.675 ± 0.049 Mpc.

Although the distance is robust, its uncertainty remains a dominant source of systematic error in our final black hole mass. Since M_{BH} scales linearly with distance ($M_{\text{BH}} \propto D$), the ± 0.049 Mpc uncertainty from the NED average and ± 0.14 Mpc uncertainty from our adopted distance propagate to systematic uncertainties of $\pm 1.3\%$ and 2.9% in our M_{BH} measurement, respectively. This is comparable to the formal statistical errors from our dynamical models and thus represents a key component of the total error budget.

5.3.2. AGN-Contaminated Stellar Mass Model

We evaluated the impact of the *HST* AGN contamination on the M_{BH} and M/L_J measurements by replacing our best-fitting, combined, and AGN-free MGE model (Table 3) by the similar best-fitting and combined but AGN-contaminated MGE model (Section 3.5), which is shown in black line in the right panel of Figure 8. The enclosed luminosity difference within $1''$ between the AGN-free and AGN-contaminated MGE models is $8.5 \times 10^6 L_{\odot}$. Adopting the constant M/L_J from either the JAM_{cyl} or JAM_{sph} models, this corresponds to a stellar mass difference of $(1.4\text{--}1.5) \times 10^7 M_{\odot}$, introducing a $\sim(11\text{--}20)\%$ uncertainty in the M_{BH} estimates under the fixed M/L_J and anisotropy values as presented in Table 4.

More realistic tests allowed both M_{BH} and M/L_J to vary in the JAM_{cyl} and JAM_{sph} models using the AGN-contaminated MGE model. The best-fitting JAM_{cyl} model with constant M/L_J yields $M_{\text{BH}} = (4.26 \pm 0.21) \times 10^7 M_{\odot}$ and $M/L_J = 1.79 \pm 0.03 (M_{\odot}/L_{\odot})$, while the corresponding JAM_{sph} model gives $M_{\text{BH}} = (3.81 \pm 0.36) \times 10^7 M_{\odot}$ and $M/L_J = 1.49 \pm 0.09 (M_{\odot}/L_{\odot})$. All other parameters differ by less than 8% from the values in Table 4 and are discussed in Section 5.1. The close agreement with the results obtained using the AGN-free MGE model indicates that AGN light in the central region, adding to the stellar mass, introduces uncertainty in the M_{BH} estimates.

5.3.3. Alternative Stellar Kinematic Measurements

We additionally derived the stellar kinematics of M81 from the NIRSpec G235H/F170LP data using an alternative setup

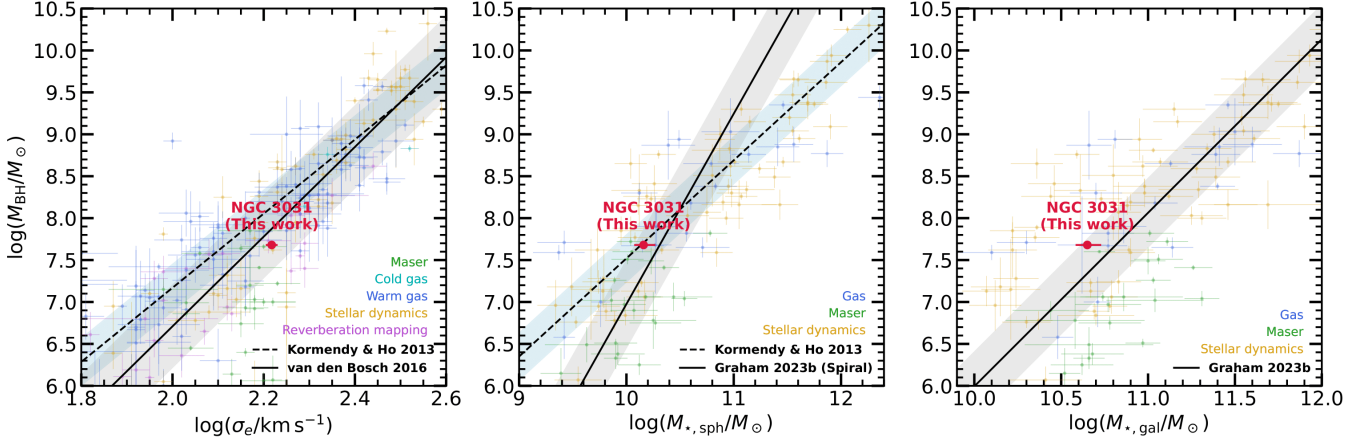


Figure 14. Location of M81 with respect to the $M_{\text{BH}}-\sigma$ (left), $M_{\text{BH}}-M_{\star,\text{sph}}$ (middle), $M_{\text{BH}}-M_{\star,\text{gal}}$ (right) scaling relation. Our new measurements are consistent within 1σ with the $M_{\text{BH}}-\sigma$ scaling relations for spiral galaxies.

based on the higher-resolution PHOENIX synthetic stellar library (Section 2.4; T.-O. Husser et al. 2013) and adopting `moments` = 2 in pPXF. The resulting kinematics are consistent with our fiducial measurements, which employ the XSL library with `moments` = 2, to within 3%. We evaluated the impact of these alternative kinematic measurements on the inferred M_{BH} and M/L_J and find that the resulting systematic differences are negligible.

5.4. M_{BH} -Galaxy Scaling Relations

We examine the location of the central SMBH in M81 relative to the established $M_{\text{BH}}-\sigma$, $M_{\text{BH}}-M_{\star,\text{sph}}$, and $M_{\text{BH}}-M_{\star,\text{gal}}$ scaling relations. We adopt a stellar velocity dispersion of $\sigma_e = (165 \pm 4) \text{ km s}^{-1}$, measured outside the SMBH's SOI, along with stellar mass estimates of $\log(M_{\star,\text{sph}}) = (10.16 \pm 0.11) M_{\odot}$ for the spheroidal component (B. L. Davis et al. 2019) and $\log(M_{\star,\text{gal}}) = (10.65 \pm 0.08) M_{\odot}$ for the total galaxy (B. L. Davis et al. 2018). Using these values, we placed M81 on the $M_{\text{BH}}-\sigma$ relations from J. Kormendy & L. C. Ho (2013) and R. C. E. van den Bosch (2016) (see Figure 14), as well as on the $M_{\text{BH}}-M_{\star,\text{sph}}$ and $M_{\text{BH}}-M_{\star,\text{gal}}$ relations from J. Kormendy & L. C. Ho (2013) and A. W. Graham & N. Sahu (2023). The relations presented by J. Kormendy & L. C. Ho (2013) and R. C. E. van den Bosch (2016) combine spiral, lenticular, and elliptical galaxies, whereas A. W. Graham & N. Sahu (2023) provides morphology-dependent fits; for the latter, we adopt the spiral-galaxy relations. The black hole masses used to define these scaling relations are predominantly derived from dynamical measurements based on gas, maser, and stellar kinematics; in the case of the $M_{\text{BH}}-\sigma$ relation, they are additionally included black hole masses obtained via reverberation mapping.

Our measured M_{BH} for M81 is consistent within 1σ of the R. C. E. van den Bosch (2016) $M_{\text{BH}}-\sigma$ relation and within 2σ of the J. Kormendy & L. C. Ho (2013) relation. Similarly, M81 lies within 1σ of both the J. Kormendy & L. C. Ho (2013) and A. W. Graham & N. Sahu (2023) $M_{\text{BH}}-M_{\star,\text{sph}}$

relations, as well as the A. W. Graham & N. Sahu (2023) $M_{\text{BH}}-M_{\star,\text{gal}}$ relation.

6. CONCLUSIONS

We have presented the first robust stellar-dynamical measurement of the SMBH mass in the nearby spiral galaxy M81. Previous determinations were unreliable, being based on disturbed gas kinematics or preliminary stellar-dynamical models. Our analysis leverages the power of JWST/NIRSpec IFU observations, which provide high-resolution 2D stellar kinematics in the NIR, allowing us to penetrate the dusty nucleus and cleanly separate stellar light from the AGN continuum. Our main results are as follows:

1. The NIRSpec data clearly resolve the BH's SOI. We measured a sharp rise in the stellar velocity dispersion from 165 km s^{-1} at large radii to a central peak of $233 \pm 15 \text{ km s}^{-1}$, providing unambiguous kinematic evidence for a central dark mass.
2. We performed a comprehensive dynamical analysis using an ensemble of 12 JAM models to systematically account for uncertainties in the instrumental PSF, stellar- M/L ratio, and orbital anisotropy. This robust approach yields a black hole mass of $M_{\text{BH}} = (4.78^{+0.07}_{-0.10}) \times 10^7 M_{\odot}$.
3. Our models confirm the expected mass-anisotropy degeneracy, where more tangentially biased orbits require a more massive black hole. Our Bayesian framework fully explores this degeneracy, and its effect is incorporated into our final quoted uncertainties.
4. This new, reliable mass measurement for M81 resolves a long-standing uncertainty. It provides a crucial anchor point for SMBH-galaxy scaling relations, particularly for spiral galaxies, where it is consistent with the established $M_{\text{BH}}-\sigma$ and $M_{\text{BH}}-M_{\star,\text{gal}}$ relations.

ACKNOWLEDGEMENTS

N.T. would like to acknowledge partial support from UKRI grant ST/X002322/1 for UK ELT Instrument Development at Oxford. M.P. acknowledges support through the grants PID2021-127718NB-I00 and RYC2023-044853-I, funded by the Spanish Ministry of Science and Innovation/State Agency of Research MCIN/AEI/10.13039/501100011033 and El Fondo Social Europeo Plus FSE+. M.P.S. acknowledges support under grants RYC2021-033094-I, CNS2023-145506, and PID2023-146667NB-I00 funded by MCIN/AEI/10.13039/501100011033 and the European Union NextGenerationEU/PRTR.

This research is based on observations made with the NASA/ESA Hubble Space Telescope obtained from the Space Telescope Science Institute, which is operated by the Association of Universities for Research in Astronomy, Inc., under NASA contract NAS 5-26555. This work is based [in part] on observations made with the NASA/ESA/CSA James Webb Space Telescope. The data were obtained from the Mikulski

Archive for Space Telescopes at the Space Telescope Science Institute, which is operated by the Association of Universities for Research in Astronomy, Inc., under NASA contract NAS 5-03127 for *JWST*. These observations are associated with program #02016.

Some/all of the data presented in this article were obtained from the Mikulski Archive for Space Telescopes (MAST) at the Space Telescope Science Institute. The specific observations analyzed can be accessed via [doi:10.17909/cbpe-ft90](https://doi.org/10.17909/cbpe-ft90).

Facility: *JWST/NIRSpec, HST/WFC3, and 2MASS.*

Software: Python 3.12 ([G. Van Rossum & F. L. Drake 2009](https://doi.org/10.5281/zenodo.1482960)), Matplotlib 3.6 ([J. D. Hunter 2007](https://doi.org/10.5281/zenodo.1482961)), NumPy 1.22 ([C. R. Harris et al. 2020](https://doi.org/10.5281/zenodo.1482962)), SciPy 1.3 ([P. Virtanen et al. 2020](https://doi.org/10.5281/zenodo.1482963)), photutils 0.7 ([L. Bradley et al. 2024](https://doi.org/10.5281/zenodo.1482964)), AstroPy 5.1 ([Astropy Collaboration et al. 2022](https://doi.org/10.5281/zenodo.1482965)), AdaMet 2.0 ([M. Cappellari et al. 2013](https://doi.org/10.5281/zenodo.1482966)), JamPy 7.2 ([M. Cappellari 2020](https://doi.org/10.5281/zenodo.1482967)), pPXF 8.2 ([M. Cappellari 2023](https://doi.org/10.5281/zenodo.1482968)), vorbin 3.1 ([M. Cappellari & Y. Copin 2003](https://doi.org/10.5281/zenodo.1482969)), and MgeFit 5.0 ([M. Cappellari 2002](https://doi.org/10.5281/zenodo.1482970)).

REFERENCES

Ahn, C. P., Seth, A. C., Cappellari, M., et al. 2018, *ApJ*, 858, 102, doi: [10.3847/1538-4357/aabc57](https://doi.org/10.3847/1538-4357/aabc57)

Astropy Collaboration, Price-Whelan, A. M., Lim, P. L., et al. 2022, *ApJ*, 935, 167, doi: [10.3847/1538-4357/ac7c74](https://doi.org/10.3847/1538-4357/ac7c74)

Barth, A. J., Sarzi, M., Rix, H.-W., et al. 2001, 555, 685, doi: [10.1086/321523](https://doi.org/10.1086/321523)

Batcheldor, D., Robinson, A., Axon, D. J., Perlman, E. S., & Merritt, D. 2010, *ApJL*, 717, L6, doi: [10.1088/2041-8205/717/1/L6](https://doi.org/10.1088/2041-8205/717/1/L6)

Bender, R., Saglia, R. P., & Gerhard, O. E. 1994, *MNRAS*, 269, 785, doi: [10.1093/mnras/269.3.785](https://doi.org/10.1093/mnras/269.3.785)

Bentz, M. C. 2025, *Research Notes of the American Astronomical Society*, 9, 128, doi: [10.3847/2515-5172/adddac](https://doi.org/10.3847/2515-5172/adddac)

Binney, J., & Mamon, G. A. 1982, *MNRAS*, 200, 361, doi: [10.1093/mnras/200.2.361](https://doi.org/10.1093/mnras/200.2.361)

Bower, G. A., Wilson, A. S., Heckman, T. M., et al. 2000, in *American Astronomical Society Meeting Abstracts*, Vol. 197, *American Astronomical Society Meeting Abstracts*, 92.03. <https://ui.adsabs.harvard.edu/abs/2000AAS...197.9203B>

Bradley, L., Sipőcz, B., Robitaille, T., et al. 2024, 2.0.2 Zenodo, doi: [10.5281/zenodo.13989456](https://doi.org/10.5281/zenodo.13989456)

Bushouse, H., Eisenhamer, J., Dencheva, N., et al. 2024, 1.14.0 Zenodo, doi: [10.5281/zenodo.10870758](https://doi.org/10.5281/zenodo.10870758)

Cappellari, M. 2002, *MNRAS*, 333, 400, doi: [10.1046/j.1365-8711.2002.05412.x](https://doi.org/10.1046/j.1365-8711.2002.05412.x)

Cappellari, M. 2008, *MNRAS*, 390, 71, doi: [10.1111/j.1365-2966.2008.13754.x](https://doi.org/10.1111/j.1365-2966.2008.13754.x)

Cappellari, M. 2017, *MNRAS*, 466, 798, doi: [10.1093/mnras/stw3020](https://doi.org/10.1093/mnras/stw3020)

Cappellari, M. 2020, *MNRAS*, 494, 4819, doi: [10.1093/mnras/staa959](https://doi.org/10.1093/mnras/staa959)

Cappellari, M. 2023, *MNRAS*, 526, 3273, doi: [10.1093/mnras/stad2597](https://doi.org/10.1093/mnras/stad2597)

Cappellari, M. 2026, in *Encyclopedia of Astrophysics*, Volume 4, ed. I. Mandel, Vol. 4 (Amsterdam, The Netherlands: Elsevier), 122–152, doi: [10.1016/B978-0-443-21439-4.00109-7](https://doi.org/10.1016/B978-0-443-21439-4.00109-7)

Cappellari, M., & Copin, Y. 2003, *MNRAS*, 342, 345, doi: [10.1046/j.1365-8711.2003.06541.x](https://doi.org/10.1046/j.1365-8711.2003.06541.x)

Cappellari, M., & Emsellem, E. 2004, *PASP*, 116, 138, doi: [10.1086/381875](https://doi.org/10.1086/381875)

Cappellari, M., Neumayer, N., Reunanen, J., et al. 2009, *MNRAS*, 394, 660, doi: [10.1111/j.1365-2966.2008.14377.x](https://doi.org/10.1111/j.1365-2966.2008.14377.x)

Cappellari, M., Scott, N., Alatalo, K., et al. 2013, *MNRAS*, 432, 1709, doi: [10.1093/mnras/stt562](https://doi.org/10.1093/mnras/stt562)

Chu, Q., Yu, S., & Lu, Y. 2022, *MNRAS*, 509, 1557, doi: [10.1093/mnras/stab2882](https://doi.org/10.1093/mnras/stab2882)

Dalcanton, J. J., Williams, B. F., Seth, A. C., et al. 2009, 183, 67, doi: [10.1088/0067-0049/183/1/67](https://doi.org/10.1088/0067-0049/183/1/67)

Davis, B. L., Graham, A. W., & Cameron, E. 2018, *ApJ*, 869, 113, doi: [10.3847/1538-4357/aae820](https://doi.org/10.3847/1538-4357/aae820)

Davis, B. L., Graham, A. W., & Cameron, E. 2019, *ApJ*, 873, 85, doi: [10.3847/1538-4357/aaf3b8](https://doi.org/10.3847/1538-4357/aaf3b8)

Davis, T. A., Bureau, M., Cappellari, M., Sarzi, M., & Blitz, L. 2013, *Nature*, 494, 328, doi: [10.1038/nature11819](https://doi.org/10.1038/nature11819)

Davis, T. A., Nguyen, D. D., Seth, A. C., et al. 2020, *MNRAS*, 496, 4061, doi: [10.1093/mnras/staa1567](https://doi.org/10.1093/mnras/staa1567)

D'Eugenio, F., Perez-Gonzalez, P., Maiolino, R., et al. 2023, <https://arxiv.org/abs/2308.06317>

D'Eugenio, F., Pérez-González, P. G., Maiolino, R., et al. 2024, *NaAs*, 8, 1443, doi: [10.1038/s41550-024-02345-1](https://doi.org/10.1038/s41550-024-02345-1)

D'Eugenio, F., Juodžbalis, I., Ji, X., et al. 2025, arXiv e-prints, arXiv:2506.14870, doi: [10.48550/arXiv.2506.14870](https://doi.org/10.48550/arXiv.2506.14870)

Devereux, N., Ford, H., Tsvetanov, Z., & Jacoby, G. 2003, *AJ*, 125, 1226, doi: [10.1086/367595](https://doi.org/10.1086/367595)

Drehmer, D. A., Storchi-Bergmann, T., Ferrari, F., Cappellari, M., & Riffel, R. A. 2015, *MNRAS*, 450, 128, doi: [10.1093/mnras/stv536](https://doi.org/10.1093/mnras/stv536)

Durrell, P. R., Sarajedini, A., & Chandar, R. 2010, *ApJ*, 718, 1118, doi: [10.1088/0004-637X/718/2/1118](https://doi.org/10.1088/0004-637X/718/2/1118)

Emsellem, E., Monnet, G., & Bacon, R. 1994, *A&A*, 285, 723

Eracleous, M., Hwang, J. A., & Flohic, H. M. L. G. 2010, *ApJS*, 187, 135, doi: [10.1088/0067-0049/187/1/135](https://doi.org/10.1088/0067-0049/187/1/135)

Ferrarese, L., Mould, J. R., Kennicutt, Jr., R. C., et al. 2000, 529, 745, doi: [10.1086/308309](https://doi.org/10.1086/308309)

Freedman, W. L., Hughes, S. M., Madore, B. F., et al. 1994, 427, 628, doi: [10.1086/174172](https://doi.org/10.1086/174172)

Gebhardt, K., Richstone, D., Tremaine, S., et al. 2003, *ApJ*, 583, 92, doi: [10.1086/345081](https://doi.org/10.1086/345081)

Graham, A. W., & Sahu, N. 2023, *MNRAS*, 520, 1975, doi: [10.1093/mnras/stad087](https://doi.org/10.1093/mnras/stad087)

Gültekin, K., Richstone, D. O., Gebhardt, K., et al. 2009, *ApJ*, 698, 198, doi: [10.1088/0004-637X/698/1/198](https://doi.org/10.1088/0004-637X/698/1/198)

Haario, H., Saksman, E., & Tamminen, J. 2001, *Bernoulli*, 7, 223

Harris, C. R., Millman, K. J., van der Walt, S. J., et al. 2020, *Nature*, 585, 357, doi: [10.1038/s41586-020-2649-2](https://doi.org/10.1038/s41586-020-2649-2)

Hunter, J. D. 2007, *Computing In Science & Engineering*, 9, 90, doi: [10.1109/MCSE.2007.55](https://doi.org/10.1109/MCSE.2007.55)

Husser, T.-O., Wende-von Berg, S., Dreizler, S., et al. 2013, *A&A*, 553, A6, doi: [10.1051/0004-6361/201219058](https://doi.org/10.1051/0004-6361/201219058)

Jarrett, T. H., Chester, T., Cutri, R., Schneider, S. E., & Huchra, J. P. 2003, *AJ*, 125, 525, doi: [10.1086/345794](https://doi.org/10.1086/345794)

Kormendy, J., & Bender, R. 1999, *ApJ*, 522, 772, doi: [10.1086/307665](https://doi.org/10.1086/307665)

Kormendy, J., & Ho, L. C. 2013, *ARA&A*, 51, 511, doi: [10.1146/annurev-astro-082708-101811](https://doi.org/10.1146/annurev-astro-082708-101811)

Krajnović, D., Cappellari, M., de Zeeuw, P. T., & Copin, Y. 2006, *MNRAS*, 366, 787, doi: [10.1111/j.1365-2966.2005.09902.x](https://doi.org/10.1111/j.1365-2966.2005.09902.x)

Krajnović, D., Cappellari, M., McDermid, R. M., et al. 2018, 477, 3030, doi: [10.1093/mnras/sty778](https://doi.org/10.1093/mnras/sty778)

Krist, J. 1995, in *Astronomical Society of the Pacific Conference Series*, Vol. 77, *Astronomical Data Analysis Software and Systems IV*, ed. R. A. Shaw, H. E. Payne, & J. J. E. Hayes, 349

Krist, J. E., Hook, R. N., & Stoehr, F. 2011, in *Optical Modeling and Performance Predictions V*, ed. M. A. Kahan, Vol. 8127, *International Society for Optics and Photonics (SPIE)*, 81270J, doi: [10.1117/12.892762](https://doi.org/10.1117/12.892762)

Lauer, T. R., Faber, S. M., Ajhar, E. A., Grillmair, C. J., & Scowen, P. A. 1998, *AJ*, 116, 2263, doi: [10.1086/300617](https://doi.org/10.1086/300617)

Lauer, T. R., Faber, S. M., Gebhardt, K., et al. 2005, *AJ*, 129, 2138, doi: [10.1086/429565](https://doi.org/10.1086/429565)

Law, D. R., E. Morrison, J., Argyriou, I., et al. 2023, *AJ*, 166, 45, doi: [10.3847/1538-3881/acdddc](https://doi.org/10.3847/1538-3881/acdddc)

Lena, D., Robinson, A., Marconi, A., et al. 2014, *ApJ*, 795, 146, doi: [10.1088/0004-637X/795/2/146](https://doi.org/10.1088/0004-637X/795/2/146)

Marconi, A., Schreier, E. J., Koekemoer, A., et al. 2000, *ApJ*, 528, 276, doi: [10.1086/308168](https://doi.org/10.1086/308168)

McCommas, L. P., Macri, L. M., Rejkuba, M., et al. 2009, 185, 1, doi: [10.1088/0067-0049/185/1/1](https://doi.org/10.1088/0067-0049/185/1/1)

McConnell, N. J., & Ma, C.-P. 2013, *The Astrophysical Journal*, 764, 184, doi: [10.1088/0004-637X/764/2/184](https://doi.org/10.1088/0004-637X/764/2/184)

Milosavljević, M., & Merritt, D. 2001, *ApJ*, 563, 34, doi: [10.1086/323830](https://doi.org/10.1086/323830)

Mitzkus, M., Cappellari, M., & Walcher, C. J. 2017, *MNRAS*, 464, 4789, doi: [10.1093/mnras/stw2677](https://doi.org/10.1093/mnras/stw2677)

Müller-Sánchez, F., Comerford, J., Stern, D., & Harrison, F. A. 2016, *ApJ*, 830, 50, doi: [10.3847/0004-637X/830/1/50](https://doi.org/10.3847/0004-637X/830/1/50)

Neumayer, N., Cappellari, M., Reunanen, J., et al. 2007, *ApJ*, 671, 1329, doi: [10.1086/523039](https://doi.org/10.1086/523039)

Ngo, H. N., Nguyen, D. D., Le, T. T. Q., et al. 2025, *Universe*, 11, doi: [10.3390/universe11110360](https://doi.org/10.3390/universe11110360)

Ngo, H. N., Nguyen, D. D., Nguyen, T. N., Dang, T. H., & Ho, T. H. T. 2025a, arXiv e-prints, arXiv:2509.03364, <https://arxiv.org/abs/2509.03364>

Ngo, H. N., Nguyen, D. D., Le, T. Q. T., et al. 2025b, *ApJ*, 992, 211, doi: [10.3847/1538-4357/ae0455](https://doi.org/10.3847/1538-4357/ae0455)

Nguyen, D. D. 2017, arXiv e-prints, arXiv:1712.02470, doi: [10.48550/arXiv.1712.02470](https://doi.org/10.48550/arXiv.1712.02470)

Nguyen, D. D. 2019, in *ALMA2019: Science Results and Cross-Facility Synergies*, 106, doi: [10.5281/zenodo.3585410](https://doi.org/10.5281/zenodo.3585410)

Nguyen, D. D., Cappellari, M., & Pereira-Santalla, M. 2023, *MNRAS*, 526, 3548, doi: [10.1093/mnras/stad2860](https://doi.org/10.1093/mnras/stad2860)

Nguyen, D. D., Seth, A. C., Reines, A. E., et al. 2014, *ApJ*, 794, 34, doi: [10.1088/0004-637X/794/1/34](https://doi.org/10.1088/0004-637X/794/1/34)

Nguyen, D. D., Seth, A. C., den Brok, M., et al. 2017, *ApJ*, 836, 237, doi: [10.3847/1538-4357/aa5cb4](https://doi.org/10.3847/1538-4357/aa5cb4)

Nguyen, D. D., Seth, A. C., Neumayer, N., et al. 2018, *ApJ*, 858, 118, doi: [10.3847/1538-4357/aabe28](https://doi.org/10.3847/1538-4357/aabe28)

Nguyen, D. D., Seth, A. C., Neumayer, N., et al. 2019, *ApJ*, 872, 104, doi: [10.3847/1538-4357/aafe7a](https://doi.org/10.3847/1538-4357/aafe7a)

Nguyen, D. D., den Brok, M., Seth, A. C., et al. 2020, *ApJ*, 892, 68, doi: [10.3847/1538-4357/ab77aa](https://doi.org/10.3847/1538-4357/ab77aa)

Nguyen, D. D., Izumi, T., Thater, S., et al. 2021, *MNRAS*, 504, 4123, doi: [10.1093/mnras/stab1002](https://doi.org/10.1093/mnras/stab1002)

Nguyen, D. D., Bureau, M., Thater, S., et al. 2022, *MNRAS*, 509, 2920, doi: [10.1093/mnras/stab3016](https://doi.org/10.1093/mnras/stab3016)

Nguyen, D. D., Cappellari, M., Ngo, H. N., et al. 2025a, *AJ*, 170, 124, doi: [10.3847/1538-3881/ade9ba](https://doi.org/10.3847/1538-3881/ade9ba)

Nguyen, D. D., Ngo, H. N., Cappellari, M., et al. 2025b, arXiv e-prints, arXiv:2509.20519. <https://arxiv.org/abs/2509.20519>

Nguyen, D. D., Ngo, H. N., Le, T. Q. T., et al. 2025c, A&A, 698, L9, doi: [10.1051/0004-6361/202554672](https://doi.org/10.1051/0004-6361/202554672)

North, E. V., Davis, T. A., Bureau, M., et al. 2019, MNRAS, 490, 319, doi: [10.1093/mnras/stz2598](https://doi.org/10.1093/mnras/stz2598)

Onishi, K., Iguchi, S., Davis, T. A., et al. 2017, MNRAS, 468, 4663, doi: [10.1093/mnras/stx631](https://doi.org/10.1093/mnras/stx631)

Paturel, G., Petit, C., Prugniel, P., et al. 2003, A&A, 412, 45, doi: [10.1051/0004-6361:20031411](https://doi.org/10.1051/0004-6361:20031411)

Perna, M., Arribas, S., Marshall, M., et al. 2023, A&A, 679, A89, doi: [10.1051/0004-6361/202346649](https://doi.org/10.1051/0004-6361/202346649)

Perrin, M., Long, J., Osborne, S., et al. 2025, Zenodo, doi: [10.5281/ZENODO.15747364](https://doi.org/10.5281/ZENODO.15747364)

Rantala, A., Rawlings, A., Naab, T., Thomas, J., & Johansson, P. H. 2024, MNRAS, 535, 1202, doi: [10.1093/mnras/stae2424](https://doi.org/10.1093/mnras/stae2424)

Rizzi, L., Tully, R. B., Makarov, D., et al. 2007, 661, 815, doi: [10.1086/516829](https://doi.org/10.1086/516829)

Saglia, R. P., Opitsch, M., Erwin, P., et al. 2016, ApJ, 818, 47, doi: [10.3847/0004-637X/818/1/47](https://doi.org/10.3847/0004-637X/818/1/47)

Sasseville, G., Hlavacek-Larrondo, J., Berek, S. C., et al. 2024, The Astrophysical Journal, 978, 48, doi: [10.3847/1538-4357/ad93d4](https://doi.org/10.3847/1538-4357/ad93d4)

Schlafly, E. F., & Finkbeiner, D. P. 2011, ApJ, 737, 103, doi: [10.1088/0004-637X/737/2/103](https://doi.org/10.1088/0004-637X/737/2/103)

Schnorr Müller, A., Storchi-Bergmann, T., Riffel, R. A., et al. 2011, MNRAS, 413, 149, doi: [10.1111/j.1365-2966.2010.18116.x](https://doi.org/10.1111/j.1365-2966.2010.18116.x)

Shapiro, K. L., Cappellari, M., de Zeeuw, T., et al. 2006, MNRAS, 370, 559, doi: [10.1111/j.1365-2966.2006.10537.x](https://doi.org/10.1111/j.1365-2966.2006.10537.x)

Shi, F., Li, Z., Yuan, F., & Zhu, B. 2021, <https://arxiv.org/abs/2106.04041>

Silge, J. D., & Gebhardt, K. 2003, AJ, 125, 2809, doi: [10.1086/375324](https://doi.org/10.1086/375324)

Simon, D. A., Cappellari, M., & Hartke, J. 2024, MNRAS, 527, 2341, doi: [10.1093/mnras/stad3309](https://doi.org/10.1093/mnras/stad3309)

Smith, M. D., Bureau, M., Davis, T. A., et al. 2019, MNRAS, 485, 4359, doi: [10.1093/mnras/stz625](https://doi.org/10.1093/mnras/stz625)

Smith, M. D., Bureau, M., Davis, T. A., et al. 2021, MNRAS, 503, 5984, doi: [10.1093/mnras/stab791](https://doi.org/10.1093/mnras/stab791)

Tahmasebzadeh, B., Taylor, M. A., Valluri, M., et al. 2025, ApJL, 989, L42, doi: [10.3847/2041-8213/adf728](https://doi.org/10.3847/2041-8213/adf728)

Thater, S. 2019, in ALMA2019: Science Results and Cross-Facility Synergies, 129, doi: [10.5281/zenodo.3585459](https://doi.org/10.5281/zenodo.3585459)

Thater, S., Krajnović, D., Cappellari, M., et al. 2019, A&A, 625, A62, doi: [10.1051/0004-6361/201834808](https://doi.org/10.1051/0004-6361/201834808)

Thater, S., Lyubenova, M., Fahrion, K., et al. 2023, A&A, 675, A18, doi: [10.1051/0004-6361/202245362](https://doi.org/10.1051/0004-6361/202245362)

Thater, S., Krajnović, D., Weilbacher, P. M., et al. 2022, MNRAS, 509, 5416, doi: [10.1093/mnras/stab3210](https://doi.org/10.1093/mnras/stab3210)

Thatte, D., Dahlen, T., Barker, E., de Jong, R., & Koekemoer, A. 2009, NICMOS Data Handbook, Version 8.0, Space Telescope Science Institute, Baltimore, MD. <http://www.stsci.edu/hst/nicmos>

Thatte, N. A., Melotte, D., Neichel, B., et al. 2024, in Society of Photo-Optical Instrumentation Engineers (SPIE) Conference Series, Vol. 13096, Ground-based and Airborne Instrumentation for Astronomy X, ed. J. J. Bryant, K. Motohara, & J. R. D. Vernet, 1309614, doi: [10.1117/12.3018520](https://doi.org/10.1117/12.3018520)

Tikhonov, N. A., & Galazutdinova, O. A. 2005, 31, 228, doi: [10.1134/1.1894510](https://doi.org/10.1134/1.1894510)

van den Bosch, R. C. E. 2016, ApJ, 831, 134, doi: [10.3847/0004-637X/831/2/134](https://doi.org/10.3847/0004-637X/831/2/134)

van den Bosch, R. C. E., & van de Ven, G. 2009, MNRAS, 398, 1117, doi: [10.1111/j.1365-2966.2009.15177.x](https://doi.org/10.1111/j.1365-2966.2009.15177.x)

van der Marel, R. P. 1994, MNRAS, 270, 271, doi: [10.1093/mnras/270.2.271](https://doi.org/10.1093/mnras/270.2.271)

van der Marel, R. P., & Franx, M. 1993, ApJ, 407, 525, doi: [10.1086/172534](https://doi.org/10.1086/172534)

Van Rossum, G., & Drake, F. L. 2009, Python 3 Reference Manual (Scotts Valley, CA: CreateSpace)

Verolme, E. K., Cappellari, M., Copin, Y., et al. 2002, MNRAS, 335, 517, doi: [10.1046/j.1365-8711.2002.05664.x](https://doi.org/10.1046/j.1365-8711.2002.05664.x)

Verro, K., Trager, S. C., Peletier, R. F., et al. 2022, A&A, 660, A34, doi: [10.1051/0004-6361/202142388](https://doi.org/10.1051/0004-6361/202142388)

Virtanen, P., Gommers, R., Oliphant, T. E., et al. 2020, Nature Methods, 17, 261, doi: [10.1038/s41592-019-0686-2](https://doi.org/10.1038/s41592-019-0686-2)

Voggel, K. T., Seth, A. C., Neumayer, N., et al. 2018, ApJ, 858, 20, doi: [10.3847/1538-4357/aabae5](https://doi.org/10.3847/1538-4357/aabae5)

Walsh, J. L., van den Bosch, R. C. E., Gebhardt, K., et al. 2016, 817, 2, doi: [10.3847/0004-637X/817/1/2](https://doi.org/10.3847/0004-637X/817/1/2)

Willmer, C. N. A. 2018, ApJS, 236, 47, doi: [10.3847/1538-4365/aabfdf](https://doi.org/10.3847/1538-4365/aabfdf)